An optimal sensor placement strategy for reliable expansion of mode shapes under measurement noise and modelling error

Elsevier Editorial System(tm) for Journal of Sound and Vibration

Manuscript Draft

Manuscript Number: JSV-D-19-00654R1

Title: An optimal sensor placement strategy for reliable expansion of mode shapes under measurement noise and modelling error

Article Type: Full Length Article

Section/Category: C Measurement Techniques

Keywords: Optimal sensor placement; structural health monitoring; operational modal analysis; industrial structures

Corresponding Author: Mr. Mahesh Murugan Jaya,

Corresponding Author's Institution: Politecnico di Torino

First Author: Mahesh Murugan Jaya

Order of Authors: Mahesh Murugan Jaya; Rosario Ceravolo; Luca Zanotti Fragonara; Emiliano Matta

Abstract: Modal expansion techniques are typically used to expand the experimental modal displacements at sensor positions to all unmeasured degrees of freedom. Since in most cases, sensors can be attached only at limited locations in a structure, an expansion is essential to determine mode shapes, strains, stresses, etc throughout the structure which can be used for structural health monitoring. An expansion may also help in assessing the condition of substructures such as tanks and pipelines by using sensor data from the main structure. Most conventional sensor placement algorithms are aimed to make the modal displacements at sensor positions of different modes as linearly independent as possible. However, under the presence of modelling errors and measurement noise, an optimal location based on this criterion is not guaranteed to provide an expanded mode shape which is close to the real mode shape. In this work, expected value of normal distance between the real mode shape and the expanded mode shape is used as a measure of closeness between the two entities. Optimal sensor locations can be determined by minimizing this distance. This new criterion is applied on a simple cantilever beam and on an industrial milling tower. In both cases, by using an exhaustive search of all possible sensor configurations it was possible to find sensor locations which resulted in significant reduction in the distance when compared to a conventional optimal sensor placement strategy. Sufficiently accurate sub-optimal sequential sensor placement algorithm is also suggested as an alternative to the exhaustive search which is then compared with a genetic algorithm-based search.

An optimal sensor placement strategy for reliable expansion of mode shapes under measurement noise and modelling error

Mahesh Murugan Jaya[1*], Rosario Ceravolo[2], Luca Zanotti Fragonara[3] and Emiliano Matta[4]

[1]PhD Student, Department of Structural and Geotechnical Engineering, Politecnico di Torino, Torino, Italy and Researcher, Birla Carbon Italy SRL, Novara, Italy.

[2]Professor, Department of Structural and Geotechnical Engineering, Politecnico di Torino, Torino, Italy.

[3]Lecturer, Centre for Autonomous and Cyberphysical Systems, Cranfield University, United Kingdom.

[4]Assistant Professor, Department of Architecture and Design, Politecnico di Torino, Torino, Italy.

Abstract

Modal expansion techniques are typically used to expand the experimental modal displacements at sensor positions to all unmeasured degrees of freedom. Since in most cases, sensors can be attached only at limited locations in a structure, an expansion is essential to determine mode shapes, strains, stresses, etc throughout the structure which can be used for structural health monitoring. An expansion may also help in assessing the condition of substructures such as tanks and pipelines by using sensor data from the main structure. Most conventional sensor placement algorithms are aimed to make the modal displacements at sensor positions of different modes as linearly independent as possible. However, under the presence of modelling errors and measurement noise, an optimal location based on this criterion is not guaranteed to provide an expanded mode shape which is close to the real mode shape. In this work, expected value of normal distance between the real mode shape and the expanded mode shape is used as a measure of closeness between the two entities. Optimal sensor locations can be determined by minimizing this distance. This new criterion is applied on a simple cantilever beam and on an industrial milling tower. In both cases, by using an exhaustive search of all possible sensor configurations it was possible to find sensor locations which resulted in significant reduction in the distance when compared to a conventional optimal sensor placement strategy. Sufficiently accurate sub-optimal sequential sensor placement algorithm is also suggested as an alternative to the exhaustive search which is then compared with a genetic algorithm-based search.

Keywords: Optimal sensor placement; structural health monitoring; operational modal analysis; industrial structures

List of symbols

$\boldsymbol{\Phi}$	Numerical mode shape
$\boldsymbol{\varphi}$	Real mode shape
$\boldsymbol{\psi}$	Experimental mode shape at sensor locations
$\boldsymbol{\Psi}$	Expanded experimental mode shape
$\mathbf{C}$	Transformation matrix for modal expansion
$\mathbf{S}$	Optimal sensor configuration
$\mathbf{I}_n$	Identity matrix of size n
$\boldsymbol{\varepsilon}$	Modelling error in mode shape
$\boldsymbol{\eta}$	Measurement noise in mode shape
σ	Standard deviation of a probability density function
μ	Mean of a probability density function
n	Total number of degrees of freedom

*Corresponding author.
E-mail addresses: mahesh.murugan@polito.it, rosario.ceravolo@polito.it, l.zanottifragonara@cranfield.ac.uk, emiliano.matta@polito.it

s	Number of sensors used
r	Possible number of sensor positions
$\mathrm{Tr}(\mathbf{A})$	Trace of a square matrix $\mathbf{A}$
$\|\mathbf{X}\|_2$	Sum of squares of all elements of vector $\mathbf{X}$
C_s^r	Number of s combinations from r when the order is not important
$\mathbb{R}$	Set of real numbers

1. Introduction

Whether in conducting modal analysis tests or for structural health monitoring, a strategy for placement of sensors is of vital importance. The number of sensors which can be employed in practice is limited by factors such as cost, availability of power, accessibility of the structure, etc. Hence, the sensors which are deployed should be placed such that they maximise their intended utility. Mode shape is an important structural characteristic to be estimated for all modal analysis tests and in most health monitoring systems.

Based on the modal displacements evaluated at the sparse sensor positions, it may be required in some situations to expand the mode shapes to all structural degrees of freedom (dof). This is important as the expanded mode shapes can be used to estimate damage. For instance, Pandey et al. [1] and Kondo and Hamamoto [2] used the curvature of mode shapes as a damage indicator. An accurate estimation of mode shapes also improves estimation of stress in structural members using vibration data. Reliable estimation of stress time histories is important in fatigue analysis. Pelayo et al. [3] evaluated stresses in a simply supported glass beam and a rectangular glass plate pinned at three points using vibration data, and compared them with those estimated using strain gauges attached to some points on the structure. The estimated stresses were found to be in good agreement with those calculated from the strain gauges, which demonstrates that the methodology can be used to estimate accurate stress time-histories. A similar study to estimate stresses in an off shore truss structure under operational conditions by measuring vibrations was performed by Tarpø et al. [4]. Papadimitriou et al. [5] predicted the power spectral densities of stresses in all the locations of a truss by using vibration data obtained at the sensor positions and a dynamic model of the structure. Dertimanis et al. [6] performed a similar study to estimate stresses in a beam due to moving loads. Modal expansion can also be important in industrial structures wherein the condition of critical substructures such as tanks and pipelines need to be estimated based on the information provided by sensors attached to the main structure.

Shah and Udwadia [7,8] proposed a methodology for determining the optimal sensor location for identification of dynamic systems under the presence of measurement noise. The optimal configuration was decided as the one which minimizes covariance of the parameter to be estimated. The method was subsequently used to determine the optimal sensor configuration in order to estimate the stiffness of columns of a framed structure using vibration data. Kammer [9] introduced a method which ranks sensor locations based on their contribution to the linear independence of modal displacements. In an iterative manner, locations that do not contribute significantly are removed. The final sensor configuration tends to maximize trace and determinant of the Fisher information matrix corresponding to the target modal partitions. The method was applied to the selection of sensor locations for identification and correlation of a set of target modes for structural characterization of a large space structure. The effect of both modelling error and measurement noise was further considered in the sensor placement [10,11]. Several other criteria exist to measure the suitability of optimal sensor positions such as singular value decomposition [12] and QR decomposition [13] of the modal matrix, kinetic energy of modes at the sensor positions [14], etc. Kalman filter-based optimal sensor placement methods for state estimation in linear structural systems subjected to unmeasured excitations and noise contaminated measurements obtained by minimizing variance of the state estimate are gaining importance [15,16,17]. In the context

of state estimation, mean square error (MSE) based methods are also widely used [18,19]. An excellent overview of previously used optimal sensor placement techniques are available in Ostachowicz et al. [20], Mallardo and Aliabadi [21], Ting-Hua and Hong-Nan [22], Dongsheng [23] and Gomes et al. [24].

In conventional vibration-based monitoring of structures, accelerometers are widely used and one of the commonly used criteria to determine their optimal position involves maximising the linear independence between the modal displacement vectors of different modes reduced to the sensor positions [25]. This is usually achieved by minimizing some scalar metric corresponding to the off-diagonal elements of the Modal Assurance Criterion (MAC) [26] matrix computed at the sensor positions [25,27,28]. However, to the best of authors' knowledge, still there is no definite proof that such a criterion provides optimal configuration when a modal expansion is needed in the presence of modelling error and measurement noise. Gomes et al. [29] studied a sensor placement criterion which takes mode shape expansion into account without considering the effect of measurement noise and any modelling error present in the numerical model. Modal displacements at sensor positions was expanded using splines and subsequently compared with the complete numerical mode shape. Frobenius norm of the difference between the two mode shapes was used as an objective function for the optimization. Murugan Jaya et al. [30] studied the robustness of the conventional optimal configuration for modal expansion in the presence of modelling error and measurement noise. The similarity between expanded and real mode shapes calculated in terms of the diagonal elements of the MAC matrix between them was used as a performance criterion, and it was observed that by increasing modelling errors and noise, the correlation decreased significantly, indicating the expanded mode shape to be significantly different from the real mode shape.

In this work, a new performance metric to measure the similarity between real and expanded mode shapes under the presence of modelling error and measurement noise is introduced and then minimized using an exhaustive search of all possible sensor configurations in order to obtain the optimal sensor location. This ensures that the selected configuration is the best possible choice for modal expansion which is then compared with the conventional optimal configuration. Based on this new measure, performance of a sequential and genetic algorithm-based search method which provides optimal/sub-optimal solutions with very low computational effort is also evaluated.

2. Optimal Sensor Placement for Modal Expansion

Modal expansion techniques often use the mode shapes obtained from a numerical model in order to expand the experimental modal displacements available at the sensor position to all structural dof. However, owing to the approximations inherent in the numerical model such as incorrect modelling assumptions, unknown system dynamics, inaccurate knowledge of structural dimensions and material properties, and numerical errors due to inadequate mesh size of finite element model, numerical errors in solver, round-off errors, etc, its characteristics will always be different from that of the real structure. The resulting net discrepancy between numerical and real mode shapes is represented by $\boldsymbol{\varepsilon}$ and is hereinafter referred at as the modelling error. By using vibration data measured from the real structure using any sensor configuration $\mathbf{S}$, the corresponding experimental modal displacements can be extracted. Due to measurement noise present in the sensors and numerical errors involved in the computation of mode shapes, the calculated modal displacements will also be different from the real values. This difference in the modal displacement at sensor locations is represented by the measurement noise η.

Let $\boldsymbol{\Phi} \in \mathbb{R}^{n \times m}$ represent the mode shapes obtained from a numerical model of the structure, where n is the total number of dof and m is the number of modes considered. Let $\boldsymbol{\varphi} \in \mathbb{R}^{n \times m}$ represent the real mode shapes of the structure. The numerical mode shapes $\boldsymbol{\Phi}$ are assumed to be equal to the real mode shapes $\boldsymbol{\varphi}$ corrupted by the modelling error $\boldsymbol{\varepsilon} \in \mathbb{R}^{n \times m}$ as,

$$\boldsymbol{\Phi} = \boldsymbol{\varphi} + \boldsymbol{\varepsilon}$$

Similarly, the experimental mode shapes $\boldsymbol{\psi} \in \mathbb{R}^{s \times m}$ at the s measurement location extracted using vibration data from the real structure are assumed to be the real mode shapes of the structure at sensor locations $\boldsymbol{\varphi_s} \in \mathbb{R}^{s \times m}$ corrupted with an additive measurement noise and system identification error $\boldsymbol{\eta} \in \mathbb{R}^{s \times m}$ as,

$$\boldsymbol{\psi} = \boldsymbol{\varphi_s} + \boldsymbol{\eta}$$

The modal displacements $\boldsymbol{\psi}$ obtained at the s sensor positions can be expanded to all other dof using any modal expansion procedure. In the present study the Sequential Expansion Reduction Process (SEREP) is used as follows,

$$\boldsymbol{\Psi} = \mathbf{C}\boldsymbol{\psi} \tag{1}$$

where $\boldsymbol{\Psi} \in \mathbb{R}^{n \times m}$ is the expanded mode shape and $\mathbf{C} \in \mathbb{R}^{n \times s}$ is the transformation matrix (given in Section 2.3) for expanding displacements at the s sensor location to all n dof. $\mathbf{C}$ is dependent on the sensor configuration $\mathbf{S}$ and the numerical mode shape $\boldsymbol{\Phi}$.

The problem thus involves determination of a certain sensor configuration $\mathbf{S}$ to expand the reduced experimental modal displacements $\boldsymbol{\psi}$ using the numerical mode shapes $\boldsymbol{\Phi}$, such that the expanded mode shapes $\boldsymbol{\Psi}$ are as close as possible to the real mode shapes of the structure $\boldsymbol{\varphi}$.

2.1. Normal distance as a measure

In order to ensure that the expanded mode shapes $\boldsymbol{\Psi}$ are close to the real mode shapes of the structure $\boldsymbol{\varphi}$, a quantitative scalar measure of similarity is required. Consider a n dimensional coordinate system with axes being the dof of the structure. For any mode l, the real mode shape $\boldsymbol{\varphi^l} \in \mathbb{R}^{n \times 1}$ and the expanded experimental mode shape $\boldsymbol{\Psi^l} \in \mathbb{R}^{n \times 1}$ can be represented as two vectors in this space. Figure 1(a) shows such a system for a 2 dof system when $\boldsymbol{\varphi^l}$ and $\boldsymbol{\Psi^l}$ are distinct and Fig. 1(b) depicts them when they are identical but with different scaling. Similarity between these vectors can be quantified measuring either the angle or the distance between them. The diagonal elements of MAC matrix calculated between $\boldsymbol{\varphi}$ and $\boldsymbol{\Psi}$ denotes the angle between them, while distance can be measured either in terms of the Euclidean distance or the normal distance. If the error between the vectors is given by $e = \varphi^l - \Psi^l$, the Euclidean distance $\|\varphi^l - \Psi^l\|$ is proportional to the square root of the mean square error (MSE) between the vectors, and sensor placement based on this criterion was previously used by Zhang et al. [18] and Papadimitriou et al. [19] to estimate stresses, strains, displacements, etc. MSE is dependent on the scaling of vectors $\boldsymbol{\Psi^l}$ and $\boldsymbol{\varphi^l}$ and since mode shapes are independent of scaling, in order to use MSE it should be ensured that both these vectors are scaled identically. It follows from Fig. 1(b) that even when $\boldsymbol{\Psi^l}$ and $\boldsymbol{\varphi^l}$ are identical but with different scaling, MSE is not 0 while the normal distance $\|\varphi^l - \lambda_c\Psi^l\|$ reduces to 0. The main advantage of using the normal distance $\|\varphi^l - \lambda_c\Psi^l\|$ is that it allows for obtaining a closed form solution under the assumed measurement noise and modelling errors. Thus, the optimal sensor configuration is the one which minimizes the normal distance between the two vectors. Since both the vectors are defined stochastically, the expected value of the normal distance is used for optimization.

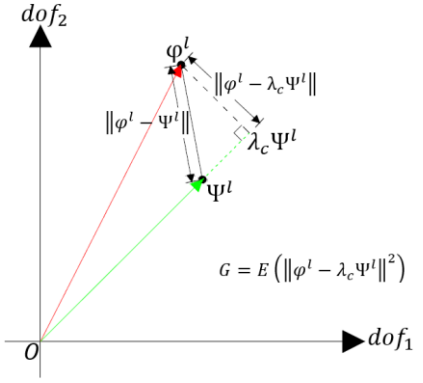

(a)

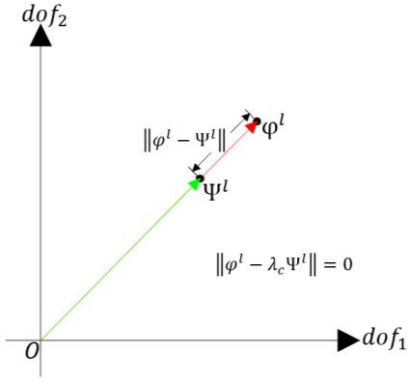

(b)

Fig. 1 Representation of real and expanded experimental mode shape ($\boldsymbol{\varphi}^{\mathbf{l}}$ and $\boldsymbol{\Psi}^{\mathbf{l}}$) in a coordinate system with degrees of freedom as axes for a two degree of freedom system when (a) $\boldsymbol{\varphi}^{\mathbf{l}}$ and $\boldsymbol{\Psi}^{\mathbf{l}}$ are different and (b) $\boldsymbol{\varphi}^{\mathbf{l}}$ and $\boldsymbol{\Psi}^{\mathbf{l}}$ are identical but with different scaling

The expected value of the square of the normal distance G for a particular sensor configuration $\mathbf{S}$ and vectors $\boldsymbol{\varphi}^{\boldsymbol{l}}$ and $\boldsymbol{\Psi}^{\boldsymbol{l}}$ is given by,

$$G = \mathrm{E}\left(\boldsymbol{\varphi}^{\boldsymbol{l}^T}\boldsymbol{\varphi}^{\boldsymbol{l}}\right) - \frac{\left(\mathrm{E}\left(\boldsymbol{\varphi}^{\boldsymbol{l}^T}\boldsymbol{\Psi}^{\boldsymbol{l}}\right)\right)^2}{\mathrm{E}\left(\boldsymbol{\Psi}^{\boldsymbol{l}^T}\boldsymbol{\Psi}^{\boldsymbol{l}}\right)} \tag{2}$$

The derivation of G is shown in Appendix-A. The function G will be used as an objective function in this work. A small value of this function denotes that real mode shape $\boldsymbol{\varphi}^{\mathbf{l}}$ and the expanded mode shape $\boldsymbol{\Psi}^{\boldsymbol{l}}$ are close and vice versa.

2.2. Definition of modelling error and measurement noise in mode shape

Reynders et al. [31, 32] studied uncertainties in modal displacements when using a Stochastic Subspace Identification (SSI) algorithm on acceleration data collected from a beam. The uncertainty in the mode shapes for any mode was found to be neither constant for all the degrees of freedom nor were the values at each degree of freedom clearly proportional to the corresponding modal displacement. Similarly, Döhler et al. [33, 34] obtained the confidence intervals about the mode shapes derived from the SSI algorithm in case of a bridge. Results were similar to those obtained in [31]. This confirms that the variation of errors in mode shapes from measurement noise and system identification cannot be easily generalised and represented for the different degrees of freedom.

Thus, for any mode l of the system, the modelling error $\boldsymbol{\varepsilon}^{\boldsymbol{l}}$ is assumed to be Gaussian with 0 mean, uncorrelated and with the same standard deviation σ_ε at all the n degrees of freedom. Even though Tondreau et al., [35] has shown that the errors in the identified mode shapes are correlated at some degrees of freedom, in the present study this correlation is not considered. Cumulative effects of measurement noise and errors from system identification for any mode l represented by $\boldsymbol{\eta}^{\boldsymbol{l}}$ is also assumed to be Gaussian with 0 mean, uncorrelated and with a uniform standard deviation σ_η at all sensor locations. Thus, the error (both due to modelling and measurement noise) in the mode shapes can be quantified using σ_ε and σ_η. As an example, Fig. 2 shows the 95% uncertainty bound on the real mode shape φ^l of a cantilever for different values of σ_ε when the maximum value of the numerical mode shape is normalised to one. The probability density function (pdf) which follows a normal distribution with standard deviation σ_ε is also plotted at the centre of beam. A higher value of σ_ε means higher uncertainty and vice versa.

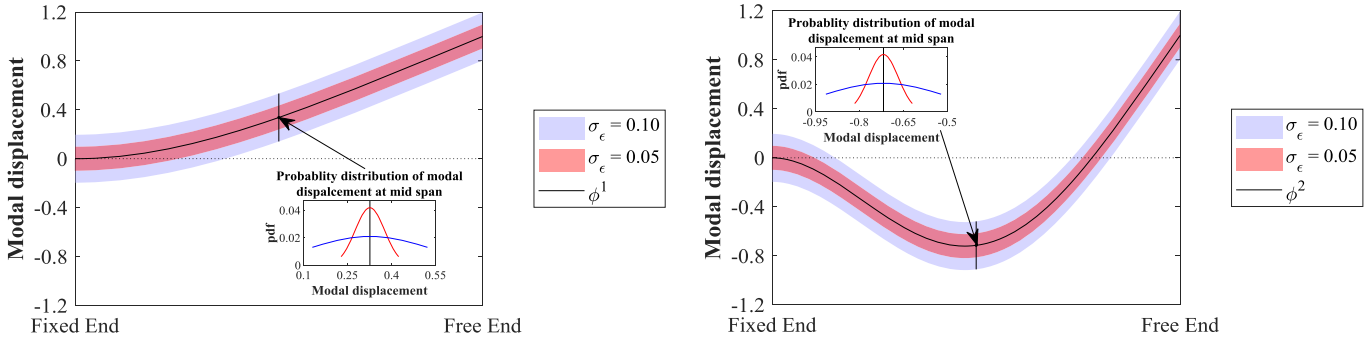

(a) **(b)**

Fig. 2 95% uncertainty bounds in real mode shape $\boldsymbol{\varphi}^{\mathbf{l}}$ with standard deviation σ_ε of 0.10 and 0.05 in case of a cantilever beam for (a) Mode-1 and (b) Mode-2

Based on the above definition of modelling error and measurement noise, Eq. (2) becomes,

$$G = n{\sigma_\varepsilon}^2 + \left\|\boldsymbol{\Phi}^{\boldsymbol{l}}\right\|_2^{\,2} - \frac{\left(\boldsymbol{\Phi}^{\boldsymbol{l}^{\mathrm{T}}}\mathbf{C}\boldsymbol{\Phi}_{\boldsymbol{s}}^{\boldsymbol{l}} + \mathrm{tr}\left(\mathrm{E}\left(\boldsymbol{\varepsilon}^{\boldsymbol{l}}\boldsymbol{\varepsilon}_{\boldsymbol{s}}^{\boldsymbol{l}^{\mathrm{T}}}\right)\mathbf{C}^{\mathrm{T}}\right)\right)^2}{\mathrm{tr}\left(\mathbf{C}{\boldsymbol{\Sigma}_{\mathbf{N}}}^2\mathbf{C}^{\mathrm{T}}\right) + \boldsymbol{\Phi}_{\boldsymbol{s}}^{\boldsymbol{l}^{\mathrm{T}}}\mathbf{C}^{\mathrm{T}}\mathbf{C}\boldsymbol{\Phi}_{\boldsymbol{s}}^{\boldsymbol{l}}} \tag{3}$$

where, $\boldsymbol{\Sigma_N}^2 = \mathbf{I_n}\sigma_N{}^2$, $\sigma_N{}^2 = \sigma_\varepsilon{}^2 + \sigma_\eta{}^2$ and $\left\|\boldsymbol{\Phi}^{\boldsymbol{l}}\right\|_2{}^2 = \boldsymbol{\Phi}^{\boldsymbol{l}^T}\boldsymbol{\Phi}^{\boldsymbol{l}}$. Appendix B shows the expected value of the individual terms in Eq. (2) which when substituted back results in Eq. (3). Even though the standard deviation of error in modal displacements σ_η due to measurement noise was assumed to be identical for all the sensors, the effect of varying amount of noises across the channels can also be analysed by using

$$\Sigma_N{}^2 = \begin{bmatrix} \sigma_\varepsilon{}^2 + \sigma_{\eta,1}{}^2 & 0 & \cdots & 0 \\ 0 & \sigma_\varepsilon{}^2 + \sigma_{\eta,2}{}^2 & \cdots & 0 \\ \vdots & \vdots & \ddots & \vdots \\ 0 & 0 & \cdots & \sigma_\varepsilon{}^2 + \sigma_{\eta,s}{}^2 \end{bmatrix}$$

where $\sigma_{\eta,1}, \sigma_{\eta,2}, \ldots, \sigma_{\eta,s}$ are the standard deviations across all the s sensors.

$\mathrm{E}\left(\boldsymbol{\varepsilon}^{\boldsymbol{l}}\boldsymbol{\varepsilon}_{\boldsymbol{s}}^{\boldsymbol{l}^T}\right) \in \mathbb{R}^{n\,x\,s}$ is a rectangular covariance matrix between the modelling error at $n\ dof$ and those at the s sensor positions. As the modelling errors between the different dof are uncorrelated, elements in the i^{th} row and j^{th} column of the matrix is defined as follows,

$$\mathrm{E}\left(\boldsymbol{\varepsilon}^{\boldsymbol{l}}\boldsymbol{\varepsilon}_{\boldsymbol{s}}^{\boldsymbol{l}^T}\right)_{i,j} = \begin{cases} 0 & i \neq j^{th}\ measured\ dofs \\ \sigma_\varepsilon{}^2 & i = j^{th}\ measured\ dofs \end{cases} \tag{4}$$

2.3. Expansion of mode shapes from sparse measurements

From the modal displacements evaluated at the sensor positions, mode shapes of the complete structure need to be estimated. For this, modal expansion has to be used and are normally performed in two ways; (a) through a geometric curve fitting using splines or other higher order polynomial functions without using any information from the numerical model or (b) based on the *a priori* information available from a numerical model. In this study, the mode shapes are expanded using information from the numerical model. Guyan static reduction/expansion [36] is one of the first available methods for reduction/expansion of any numerical model. However, due to the fact that static expansion neglect the inertia of the unmeasured dof, the mode shape predictions can be erroneous if significant mass are located at unmeasured dof [37]. This method was extended to include the full equation of motion for modal expansion which resulted in more dynamically accurate methods such as the dynamic expansion method [38]. The present study uses the System Equivalent Reduction Expansion Process (SEREP) [39], which expands the mode shapes to unmeasured dof using the complete numerical mode shapes. When the number of sensors s is higher than the number of modes m used for expansion, the transformation matrix $\mathbf{C} \in \mathbb{R}^{n\,x\,s}$ used in Eq. (1) is given by

$$\mathbf{C} = \boldsymbol{\Phi}\boldsymbol{\Phi}_\mathbf{s}{}^\dagger$$

where $\boldsymbol{\Phi}_\mathbf{s}{}^\dagger$ represents the Moore-Penrose pseudo-inverse (left hand inverse) of $\boldsymbol{\Phi}_\mathbf{s}$, which is given by

$$\boldsymbol{\Phi}_\mathbf{s}{}^\dagger = \left(\boldsymbol{\Phi}_\mathbf{s}{}^\mathrm{T}\boldsymbol{\Phi}_\mathbf{s}\right)^{-1}\boldsymbol{\Phi}_\mathbf{s}{}^\mathrm{T}$$

This expansion leads to a smoothing of the mode-shape data at sensor locations. However, when the number of sensors is equal to that of the modes used for expansion, the pseudo-inverse can be replaced by an ordinary inverse and in this case, there will not be any smoothing of the modal displacements at the sensor locations during expansion [40].

When using SEREP expansion, based on Appendix-C, Eq. (3) reduces to the following,

$$G = n\sigma_\varepsilon{}^2 + \left\|\boldsymbol{\Phi}^{\boldsymbol{l}}\right\|_2{}^2 - \frac{\left(\left\|\boldsymbol{\Phi}^{\boldsymbol{l}}\right\|_2{}^2 + \sigma_\varepsilon{}^2 m\right)^2}{\sigma_N{}^2\left(m + \mathrm{tr}\left(\boldsymbol{\Phi}_\mathbf{d}\left(\boldsymbol{\Phi}_\mathbf{s}{}^\mathrm{T}\boldsymbol{\Phi}_\mathbf{s}\right)^{-1}\boldsymbol{\Phi}_\mathbf{d}{}^\mathrm{T}\right)\right) + \left\|\boldsymbol{\Phi}^{\boldsymbol{l}}\right\|_2{}^2} \tag{5}$$

where $\boldsymbol{\Phi}_\mathbf{d}$ and $\boldsymbol{\Phi}_\mathbf{s}$ represents the numerical mode shape matrix $\boldsymbol{\Phi}$ partitioned at the unmeasured and measured dof respectively.

It can be seen from Eq. (5) that when modelling error and measurement noise become zero, G also reduces to zero. This is expected as, under the absence of any such uncertainties, the expanded mode shape $\boldsymbol{\Psi}^{\mathbf{l}}$, real mode shape $\boldsymbol{\varphi}^{\mathbf{l}}$

and the numerical mode shape $\mathbf{\Phi^l}$ coincide and thus the distance between them becomes 0. For a given σ_ε and σ_η, only the term $\mathrm{tr}\left(\mathbf{\Phi_d}\left(\mathbf{\Phi_s}^{\mathrm{T}}\mathbf{\Phi_s}\right)^{-1}\mathbf{\Phi_d}^{\mathrm{T}}\right)$ is dependent on the sensor location and thus this term governs the efficiency of each sensor configuration for modal expansion.

2.4. Optimal location based on a global search

Optimal sensor placement is a combinatorial optimization problem which involves the selection of an optimal set of s sensor positions $\mathbf{S}$ from a set of r possible sensor positions $\mathbf{R}$ ($s < r$ and $\mathbf{S} \subset \mathbf{R}$). The optimal configuration has to be chosen from a set of $\mathrm{C}_\mathrm{r}^\mathrm{s} = r!/s!/(r-s)!$ possible number of sensor configurations. When the number of possible sensor positions r is very large compared to the number of sensors s, $\mathrm{C}_\mathrm{r}^\mathrm{s}$ is of the order of $r^s/s!$. In this study, the optimal configuration for the objective function G is initially obtained by performing an exhaustive global search of all the $\mathrm{C}_\mathrm{r}^\mathrm{s}$ configurations which is later compared with those from sequential and a genetic algorithm-based integer optimization method.

In order for the sensor configuration to yield a modal expansion which is as close as possible to the real mode shape $\boldsymbol{\varphi^l}$, the optimal configuration $\mathbf{S_G}$ is calculated by minimizing the function G given in Eq. (5). The widely adopted conventional optimal sensor configuration $\mathbf{S_c}$ based on minimizing the linear independence of the modal displacements between the different modes at the sensor locations is evaluated and compared with the new optimal configuration. This is obtained by minimizing the peak off-diagonal elements of the MAC matrix evaluated for all the modes using the numerical mode shape at the sensor positions $\mathbf{\Phi_s}$. By ensuring maximum linear independence of mode shapes, the conventional optimal configuration $\mathbf{S_c}$ is the best suitable choice for identification problems. However, it often happens that, from such sensor placements a modal expansion may be essential. Besides introducing a new metric which can be used as a measure of the accuracy of expansion and thereby determine the new optimal configuration suitable for expansion, it is important to understand as to how the conventional optimal sensor configuration can perform in such cases. At the same time, even though the new configuration $\mathbf{S_G}$ provides linearly independent modes, it will not be efficient for identification problems as the conventional optimal configuration $\mathbf{S_c}$. When a sensor configuration needs to perform well both for mode shape expansion and identification, a Pareto optimization may be performed. Another alternative involves finding a new objective function which is a weighted sum of the conventional and the new objective function G. Let G_G and G_C represent the value of function G corresponding to the optimal sensor configuration $\mathbf{S_G}$ and $\mathbf{S_c}$, respectively.

It is to be noted that the function G is dependent on the mode considered and the standard deviation of both modelling error and measurement noise. However, the optimal configuration $\mathbf{S_G}$ is independent of these factors. This is because the effect of sensor configuration is identical in all the modes and thus finding the optimal configuration for a particular mode ensures that it is also optimal for other modes considered in the formulation of the transformation matrix $\mathbf{C}$. Unless mentioned explicitly, G is calculated with respect to the first mode of the structure.

2.5. Sequential and genetic algorithm-based sensor placement

Even though calculation of the optimal configuration using an exhaustive search of all possible configurations ensures that the resulting solution is globally optimal, for large value of possible sensor positions r and number of sensors s, the value of $\mathrm{C}_\mathrm{r}^\mathrm{s}$ become exponentially large. In most cases, it is required to have sensors much larger in number than the modes to be identified. In such cases, instead of performing an exhaustive search, a sequential procedure or any heuristic optimization strategy can be a promising alternative which can provide the optimal or sufficiently accurate sub-optimal results for the function G.

Sequential placement algorithm can be either of a forward or a backward type depending on whether sensors are added or removed from an initial optimal configuration. The forward sequential placement (FSP) algorithm starts by

first placing m (which is equal to the number of modes considered) sensors in the structure using an exhaustive search by evaluating all the C_r^m configurations as in Section 2.4 and choosing the configuration which minimizes G. Let $\mathbf{S_{initial}}$ be the optimal configuration of the m sensors. Now, the remaining $s-m$ sensors are placed in $s-m$ stages to the remaining $r-m$ positions. The next sensor $(m+1^{th})$ is placed such that the resulting configuration consisting of $\mathbf{S_{m+1}} = [\mathbf{S_{initial}}^T \quad s_{m+1}]^T$ minimizes G. This position $\mathbf{S_{m+1}}$ is obtained using an exhaustive search by placing the $m+1^{th}$ sensor in the remaining $r-m$ positions. Once the $m+1$ sensors are optimally placed, this process is repeated to place the remaining $s-(m+1)$ sensors in the same way. The number of sensor configurations to be evaluated is now of the order of $r^m/m!$ instead of $r^s/s!$. Along the same lines, a backward sequential placement (BSP) can also be performed by first keeping sensors at all the $r\ dof$ and then successively removing a sensor in each stage by performing an exhaustive search at each of those stage. Figure 3 shows a summary for both types of algorithms.

Both the sequential algorithms are computationally cheap. As an e.g., for placing 6 sensors in 20 possible sensor locations in order to expand 4 modes require $C_{20}^6 = 38760$ evaluations for an exhaustive search, while the FSP and BSP requires evaluating only $C_{20}^4 + (20-4) + (20-5) = 4876$ and $20+19+\cdots+8+7 = 189$ configurations, respectively. It is to be also noted that the sensor configuration resulting from sequential placement is not guaranteed to be the same as the global optimal configuration discussed in Section 2.4. However, it was observed that the results from the sequential placement are very close to the global optimal values obtained by an exhaustive search and thus are definitely suitable than the conventional optimal sensor locations for modal expansion. Let $\mathbf{S_{FSP}}$ and $\mathbf{S_{BSP}}$ be the optimal configurations obtained respectively from the FSP and the BSP algorithms and let G_{FSP} and G_{BSP} be the corresponding value of G.

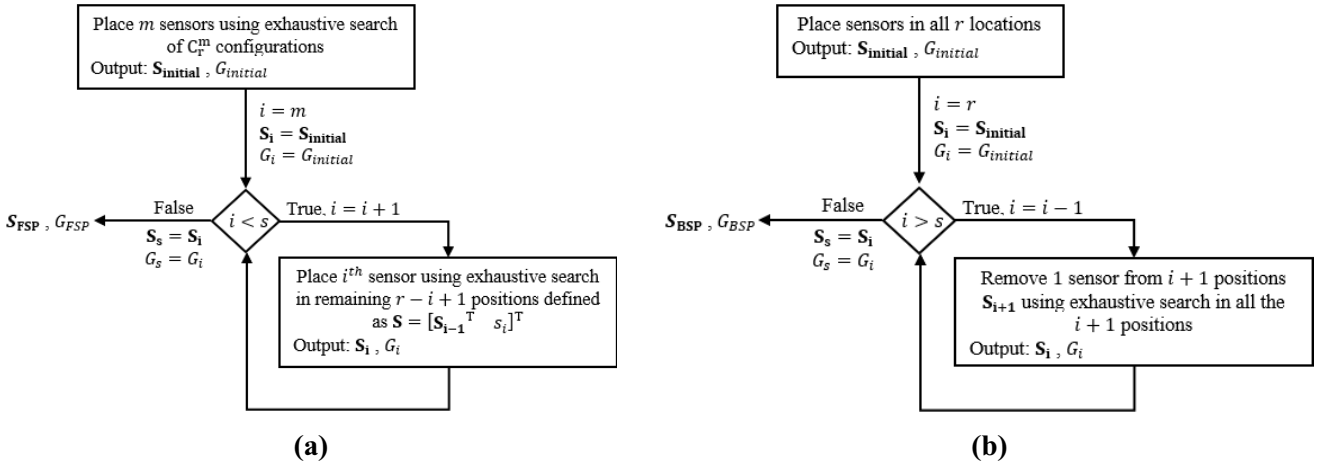

Fig. 3. Flowchart of sequential sensor placement algorithm; (a) forward sequential placement (FSP) and (b) backward sequential placement (BSP).

In the family of heuristic optimization algorithms used in sensor placement problems, genetic algorithm-based (GA) methods are widely adopted [41,42] and thus is also used in this study. The method starts by selecting a set of randomly selected initial configuration which then evolves towards the optimal configuration in each generation by means of selection, mutation and crossover [43-46]. Let $\mathbf{S_{GA}}$ represents the optimal configuration based on this method and G_{GA} denote the corresponding function G.

3. Performance Evaluation

The optimal location of sensors from the conventional MAC based sensor placement is compared with that from the new metric G by an exhaustive search of all possible configurations. For the function G, sequential and GA-based search is also performed. The performances in modal expansion between the different methods are compared first using a simple cantilever model and then with a real industrial milling tower. Smaller the function G, better is the

similarity between the expanded and the real mode shape. The decrease in the function G, when using the optimal configurations $\mathbf{S_G}$ instead of the conventional "optimal" configuration $\mathbf{S_c}$, is computed as follows,

$$I_{C,G} = \frac{G_c - G_G}{G_c} \, x \, 100 \tag{6}$$

where $I_{C,G}$ is the percentage reduction in G. Along similar lines, the reduction in G when using the sequential and GA based search is quantified using $I_{C,FSP}$, $I_{C,BSP}$ and $I_{C,GA}$ which are obtained by replacing G_G with G_{FSP}, G_{BSP} and G_{GA} respectively in equation (6). In order to assess the efficiency of the GA based sensor placement configuration when compared to the exhaustive search, the percentage difference in G between the global optimal configuration $\mathbf{S_G}$ and the genetic algorithm-based optimal configurations $\mathbf{S_{GA}}$ is evaluated as,

$$I_{GA,G} = \frac{G_{GA} - G_G}{G_{GA}} \, x \, 100 \tag{7}$$

A smaller value of $I_{GA,G}$ denotes the performance of GA to be closer to that obtained from an exhaustive global search and vice versa. Similarly, the performance of both the sequential sensor placement algorithms are measured in terms of $I_{FSP,G}$ and $I_{BSP,G}$ which can be calculated by replacing G_{GA} from equations(7) with G_{FSP} and G_{BSP}, respectively. The optimal sensor locations based on G are insensitive to the modelling error and measurement noise in the modal displacements (only when measurement noise is identical across all the sensors). However, the distance between the expanded and the real mode shape increases with an increase in both the errors. σ_ε depends on many factors such as knowledge of system dynamics, uncertainties in structure, modelling assumptions, etc while σ_η depends on quality of sensors, cables and data acquisition devices, errors arising in system identification algorithms, etc [47]. Due to such randomness, value of σ_ε and σ_η is highly problem dependent and thus cannot be generalized. This is also clear from the uncertainty bounds estimated in the SSI of modal parameters for a bridge and a building reported in Reynders et. al [31]. The obtained uncertainty bounds were found to be different for the two cases. Hence, in this study, the modal expansion performance is evaluated for different standard deviation combinations as shown in Table-1.

Table – 1. Standard deviation combinations of measurement noise and modelling error

Combination I.D.	1	2	3	4	5	6	7	8	9
σ_η	0.01	0.01	0.01	0.05	0.05	0.05	0.10	0.10	0.10
σ_ε	0.01	0.05	0.10	0.01	0.05	0.10	0.01	0.05	0.10

3.1. Cantilever beam

A 2D cantilever beam was considered, the numerical model of which was created using 100 2-noded Euler–Bernoulli beam elements. Only the translational degrees of freedom in Y direction was considered. The first four predominant modes of the beam were considered for expansion and mode shapes were scaled such that the maximum magnitude of displacement in each mode was one. 20 possible locations to place sensors which are uniformly spaced along the span of the beam was considered and are shown in Fig. 4.

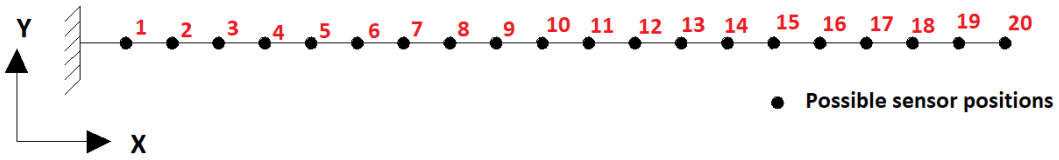

Fig. 4. Cantilever beam showing 20 possible sensor locations S to keep uniaxial accelerometers in *Y* direction

A simple case of identifying the first 2 predominant modes in Y direction using 2 sensors is initially considered. An exhaustive search of all the $C_{20}^2 = 190$ configurations was carried out to find both the optimal configurations $\mathbf{S_C}$ and

$\mathbf{S_G}$. Figure 5 shows the variation of the function G for the first mode and standard deviation combination 9 (from Table-1) with the position of both the sensors s_1 and s_2.

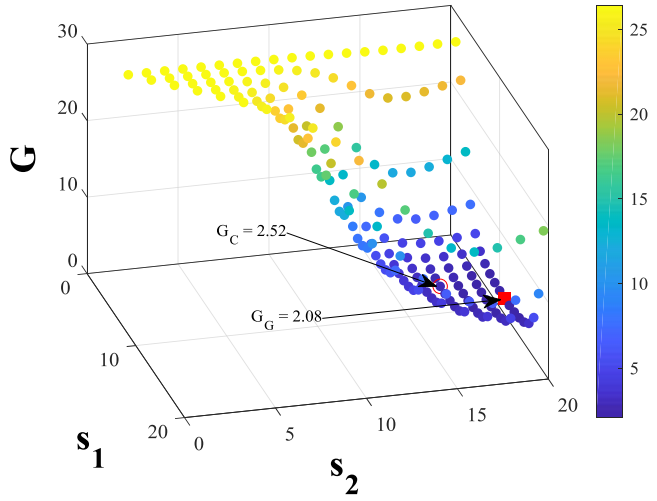

Fig. 5. Variation of G (for mode 1 and standard deviation combination 9) with sensor positions s_1 and s_2

It was found that $\mathbf{S_C} = [9 \quad 17]^T$ and $\mathbf{S_G} = [11 \quad 20]^T$ and the corresponding function G was 2.52 and 2.08, respectively. From Fig. 5, it can be seen that there are many configurations which yield reasonably low values of G (indicated in dark blue colour) while there are also configurations which result in very large G (indicated in yellow colour). In the present case, the configuration $\mathbf{S_C}$ was found in the vicinity of $\mathbf{S_G}$. This behaviour is not guaranteed for all cases and it may happen that $\mathbf{S_C}$ can result in very large G. Thus, an optimization based on G is essential. Even in this case, $I_{C,G} = 17.5\%$ which denotes a significant reduction in G.

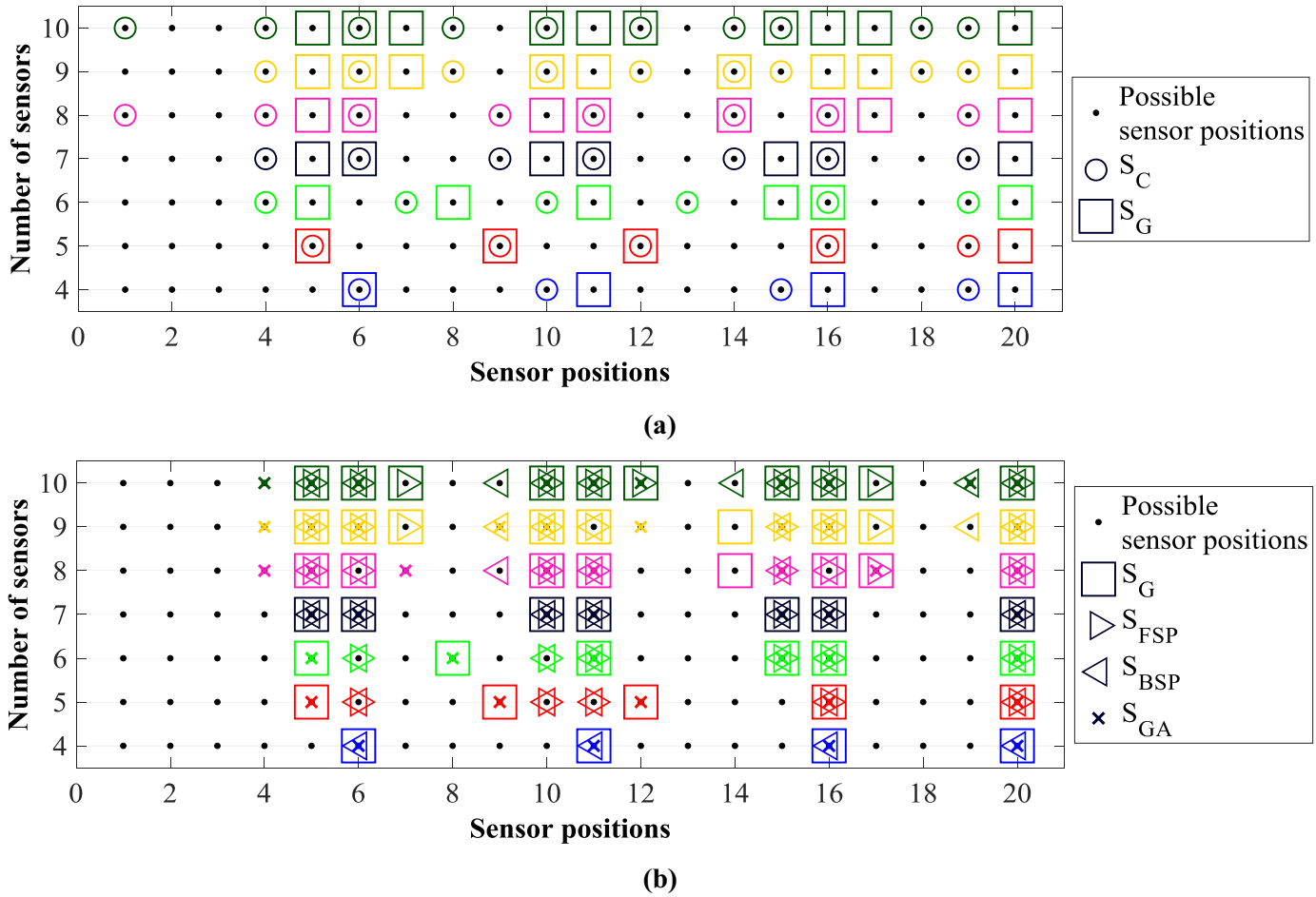

Fig. 6. Comparison of optimal configurations in case of the cantilever beam for different number of sensors; (a) $\mathbf{S_C}$ with $\mathbf{S_G}$ and (b) $\mathbf{S_G}$ with $\mathbf{S_{FSP}}$, $\mathbf{S_{BSP}}$ and $\mathbf{S_{GA}}$

Instead of two modes and two sensors considered above, a further set of simulation using 4 modes and number of sensors s ranging from 4 to 10 is now analysed to obtain the optimal configurations $\mathbf{S_C}$ and $\mathbf{S_G}$, and thus study the influence of number of sensors on mode shape expansion G. Being a theoretical study, upper limit on the number of sensors was chosen such that they are half the possible number of sensor positions as this corresponds to the case with the maximum number of possible sensor configurations. For cases where s is between 5 to 10, FSP algorithm was used to obtain the optimal configuration $\mathbf{S_{FSP}}$. BSP and GA was also used respectively in order to determine the optimal configurations $\mathbf{S_{BSP}}$ and $\mathbf{S_{GA}}$ for s between 4 to 10. Figure 6(a) shows the comparison between optimal configuration $\mathbf{S_C}$ and $\mathbf{S_G}$ while Fig. 6(b) compares $\mathbf{S_G}$ with $\mathbf{S_{FSP}}$, $\mathbf{S_{BSP}}$, and $\mathbf{S_{GA}}$.

Figure 7 shows the variation of G_C and G_G for s varying from 4 to 10. It shows that with an increase in the standard deviation of the modelling error and measurement noise, both G_C and G_G increases. It can also be seen that for any standard deviation combination, both G_C and G_G decreases with an increase in the number of sensors. As expected, G_G is less than G_C thus making the optimal configuration $\mathbf{S_G}$ to be the best choice for expansion. It is also clear from Fig. 7 that with an increase in modelling error and measurement noise, the function G increases and so does the distance between the real and the expanded mode shape. Neither the optimal configuration $\mathbf{S_G}$ nor increasing the number of sensors help in offsetting the effect of high modelling errors and standard deviation. However, given these limitations, the optimal configuration $\mathbf{S_G}$ is guaranteed to outperform the conventional optimal configuration $\mathbf{S_C}$.

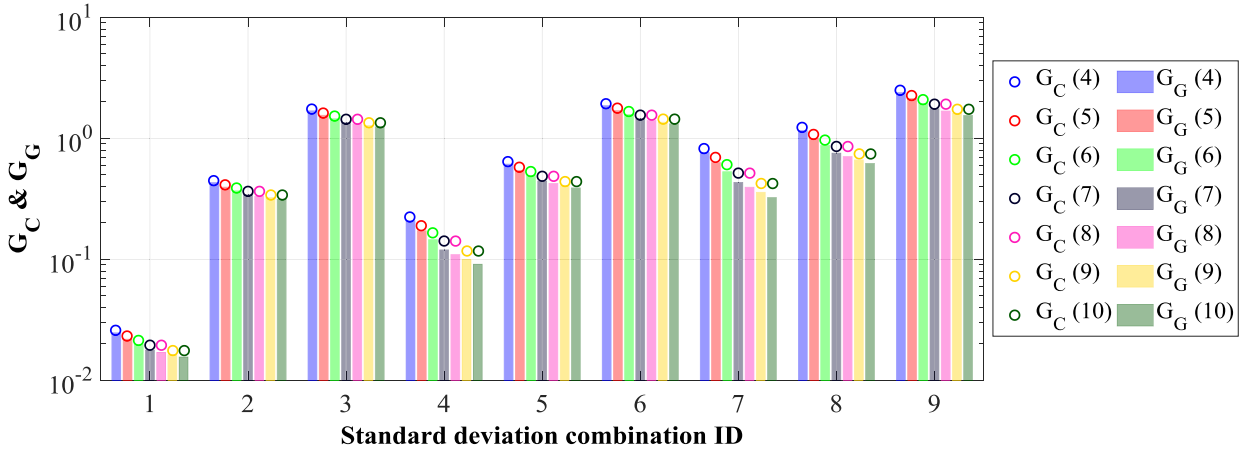

Fig. 7. Comparison of G_C and G_G in case of cantilever beam for all standard deviation combinations (number in parenthesis of G_C and G_G denote the number of sensors).

Figure 8(a) shows the variation of $I_{C,G}$, $I_{C,FSP}$, $I_{C,BSP}$ and $I_{C,GA}$ for all standard deviation combinations. $I_{C,G}$ is found to vary between 3 to 24% for the various scenarios which illustrates that the new optimal configuration $\mathbf{S_G}$ is useful in case of modal expansion than using the conventional configuration $\mathbf{S_C}$. The performance of the sequential algorithms and GA can also be seen from Fig. 9(b-d) where in the variation of $I_{FSP,G}$, $I_{BSP,G}$ and $I_{GA,G}$ is plotted for different number of sensors. The maximum value of $I_{FSP,G}$ and $I_{BSP,G}$ is around 3% and occurs when the number of sensors is 5. This may be because the difference between the optimal configurations $\mathbf{S_G}$ and sequential configurations $\mathbf{S_{FSP}}$ and $\mathbf{S_{BSP}}$ (From Fig. 6(b)) is maximum for the case of 5 sensors. In the case with 7 and 10 sensors it is seen that FSP provided the global optimal configuration $\mathbf{S_G}$ while the BSP provided the global optimal configuration for 4 and 7 number of sensors. This can be also seen from $I_{FSP,G}$ and $I_{BSP,G}$ taking 0 for these configurations. For the number of sensors between 8 and 10 sensors, $I_{FSP,G}$ and $I_{BSP,G}$ is less than 1% for all the standard deviation combinations which indicates that both the sequential algorithms are efficient for larger number of sensors. The GA method provided the true global optimal solution for s between 4 to 7. Maximum value of $I_{GA,G}$ is found to be around 4% which was reported for the case of 8 number of sensors. The sequential algorithm provides the global optimal for all values of s only if the optimal sensor configuration $\mathbf{S_G}$when using $i-1$ sensors, is a subset of the optimal configuration for the case with i sensors. While this condition cannot be ensured for all structures, it can be seen from Fig. 6(a) that some

sensors maintain their positions as the number of sensors are increased because of which the sequential method provided optimal solutions in some cases and good sub-optimal solutions in the remaining situations.

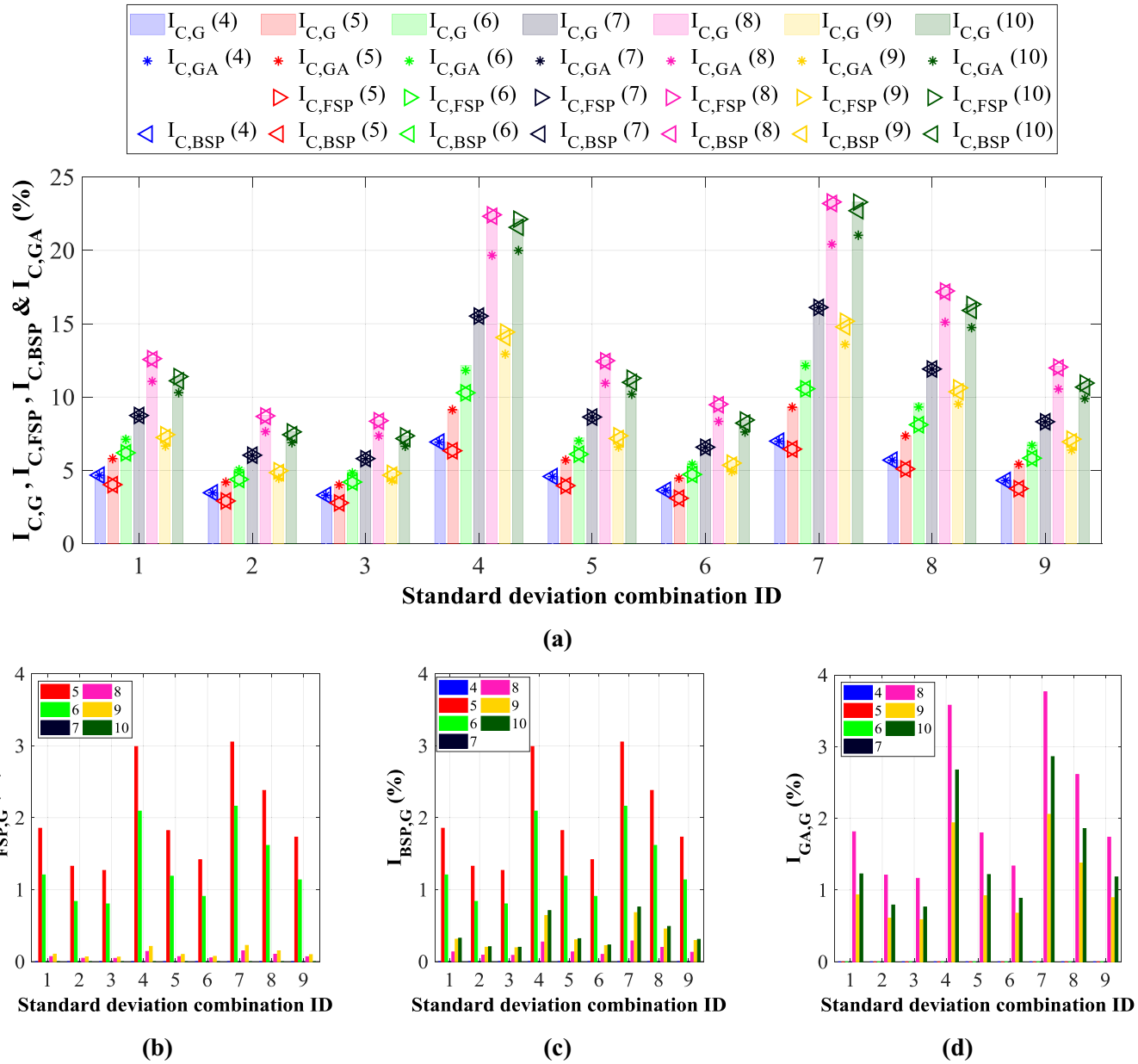

Fig. 8 Comparison of different algorithms for the cantilever beam; (a) Variation of $I_{C,G}$, $I_{C,FSP}$, $I_{C,BSP}$ and $I_{C,GA}$, (b) and (c) Variation of $I_{FSP,G}$ and $I_{BSP,G}$ respectively ($I_{FSP,G} = 0$ for $s = 7$ and 10 while $I_{BSP,G} = 0$ for $s = 4$ and 7), and (d) Variation of $I_{GA,G}$ ($I_{GA,G} = 0$ for $s = 4$ to 7).

3.2. Industrial Milling Tower

The performance of the proposed sensor placement strategy was also evaluated for an industrial tower in the Birla Carbon Italy SRL production plant in Trecate, Italy. The structure is made of steel with a floor dimension of 6 x 6.6 m and approximately 25 m tall with 7 storeys. It houses two steel tanks at a height of 20 m and 10 m from the base. Several critical pipelines and machineries are placed in the structure. This main tower is attached to a secondary tower which contains stairs. This secondary tower is 30 m tall with 10 storeys and a floor dimension of 2.5 x 4.8 m. An expansion is essential in such a structure, especially if the condition of substructures such as the two tanks or other internal pipelines needs to be estimated using sensors located on the tower. Since both the lateral modes in the structure are equally important, in this work the first two predominant modes in both X and Y directions are considered. These correspond to the first and second bending modes of the structure in X and Y directions. Figure 9(a) shows a picture of this main tower along with the secondary tower containing stairs and Fig. 9(b) shows the finite

element (FE) model of the tower along with the coordinate system. A FE model was created using 3D Euler–Bernoulli beam elements for all the beams and columns while the tanks were modelled using shell elements. The model has 10876 translational dof in X and Y direction which is considered for modal expansion. It was decided to provide an identical number of sensors in both the lateral directions. A total of 22 possible locations for the placement of uniaxial accelerometers were identified in the main tower based on accessibility and other practical constraints and are shown in Fig. 9(c). As in the case of the cantilever, the effect of sensor configurations $\mathbf{S_C}$, $\mathbf{S_G}$ and $\mathbf{S_S}$ are studied by using 4, 6, 8 and 10 sensors.

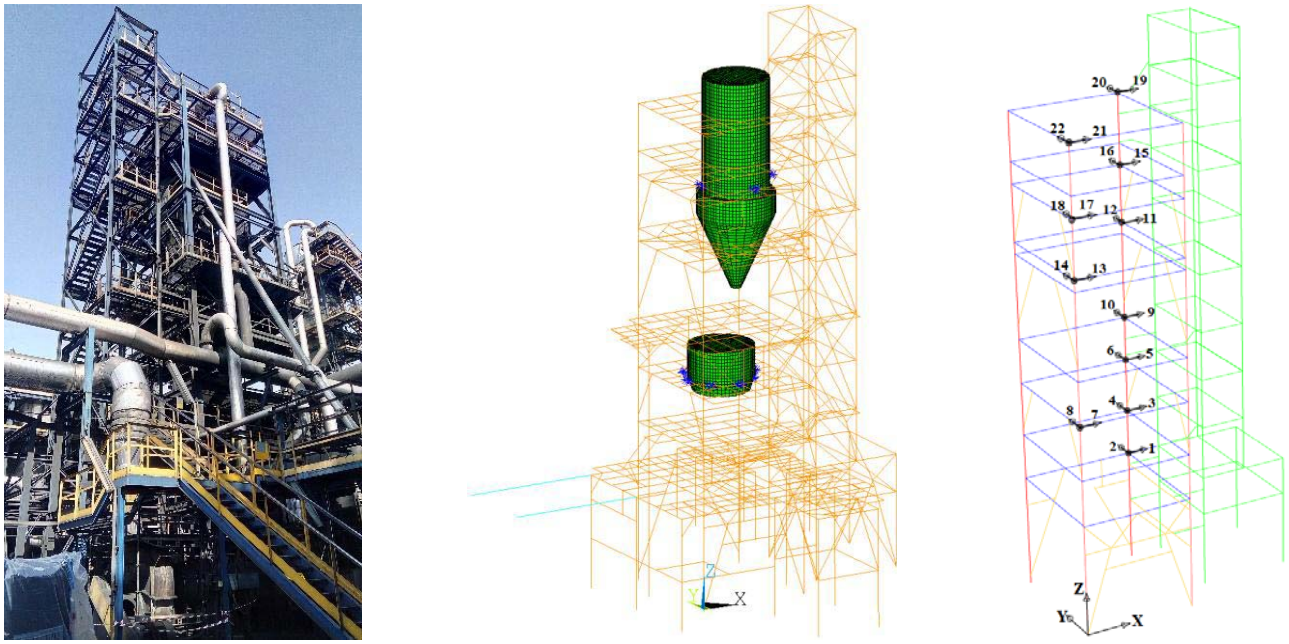

(a) **(b)** **(c)**

Fig. 9. (a) Milling tower in Birla Carbon Italy srl, (b) corresponding finite element model and (c) 22 possible locations for the placement of uniaxial sensors

The mode shapes were normalized such that the maximum displacement in the main tower was one. Figure 10 shows the comparison of the optimal configurations $\mathbf{S_C}$, $\mathbf{S_G}$, $\mathbf{S_{FSP}}$ and $\mathbf{S_{BSP}}$. Variation of both G_C and G_G for all the standard deviation combinations were similar to that of the cantilever beam and thus is not reported here.

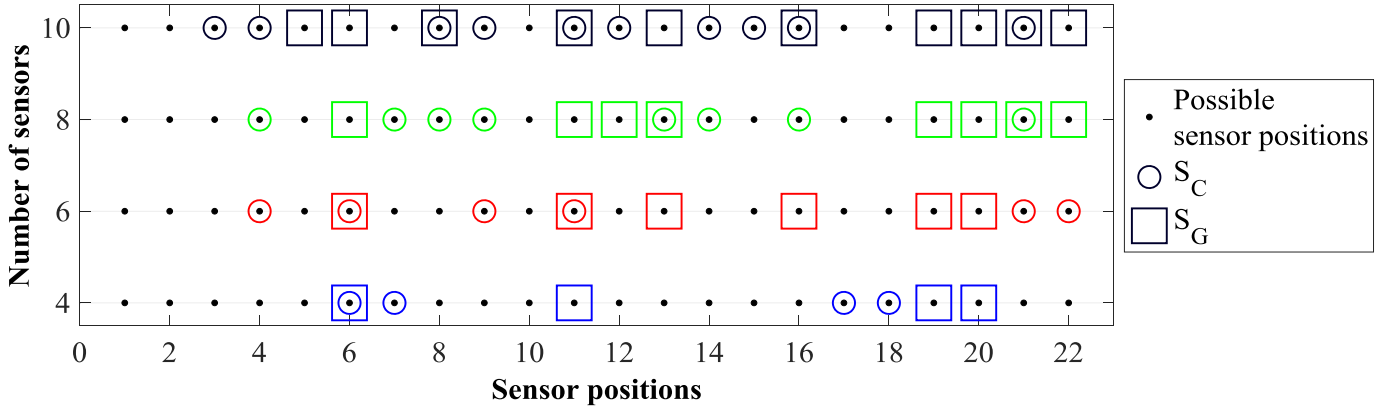

(a)

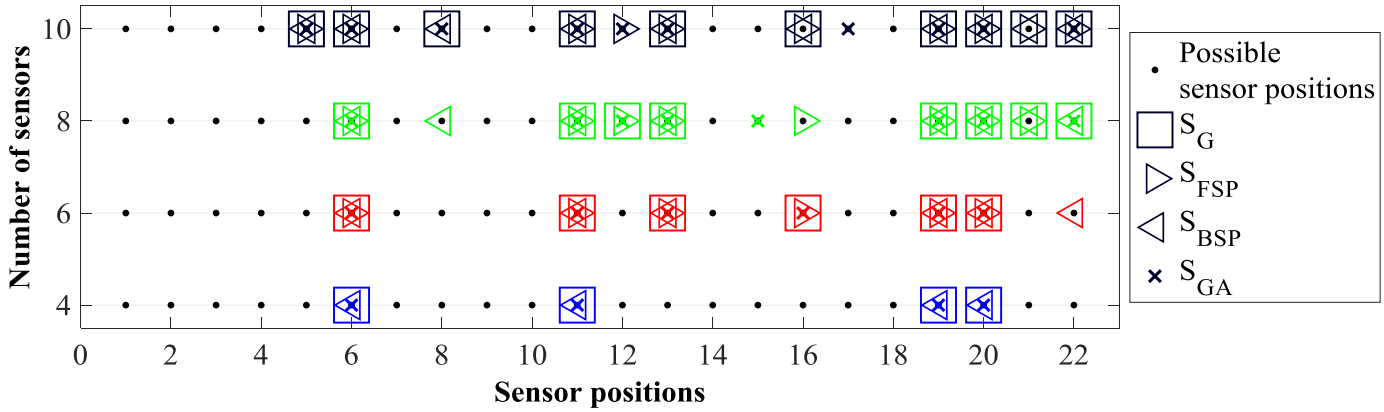

(b)

Fig. 10 Comparison of optimal configurations in case of the milling tower for different number of sensors; (a) S_C with S_G and (b) S_G with S_{FSP}, S_{BSP} and S_{GA}

Figure 11(a) shows the function $I_{C,G}$, $I_{C,FSP}$ and $I_{C,BSP}$ for all standard deviation combinations and different number of sensors. It was found that these indices ranged between 10% to 40%. This shows a significant reduction in G when compared to the conventional optimal configuration. Figure 11(b) and 11(c) shows the variation of $I_{FSP,G}$ and $I_{BSP,G}$, the maximum values of which was only around 2 % and 1 % respectively, while Fig. 11(d) depicts $I_{GA,G}$, in which case the maximum value was 4% and occurred in the case with 10 sensors. The FSP method provided the global optimal configuration only in the case with 6 sensors while the BSP method provided global optimal with 4 and 10 sensors. In spite of the fact that both the sequential methods did not result in global optimal for some scenarios, the very low values of $I_{FSP,G}$ and $I_{BSP,G}$ indicates that they can still be used. GA method provided the optimal configuration in the case with 4 and 6 sensors.

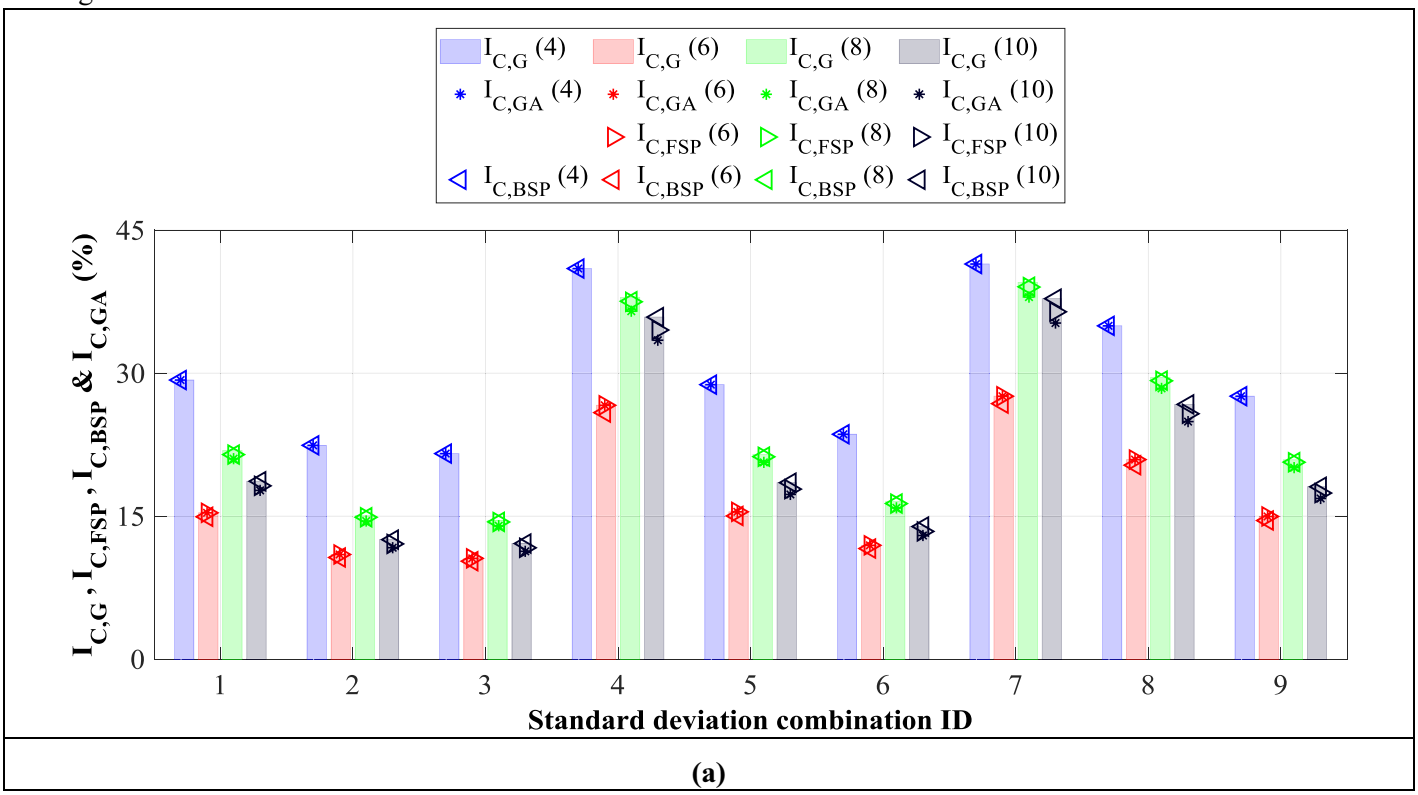

(a)

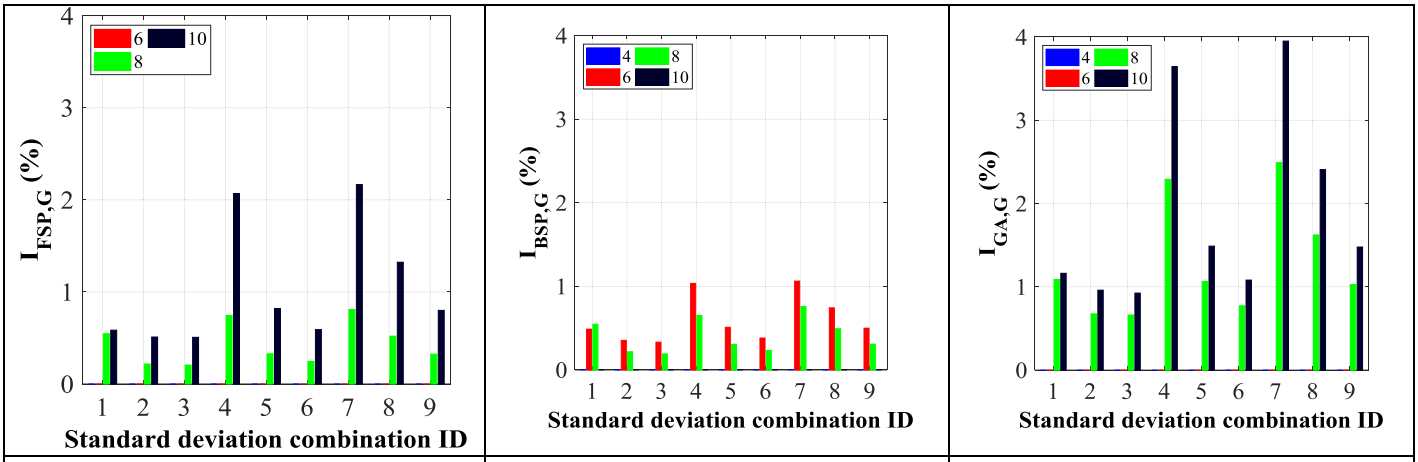

(b) (c) (d)

Fig. 11. Comparison of different algorithms for the milling tower; (a) Variation of $I_{C,G}$, $I_{C,FSP}$, $I_{C,BSP}$ and $I_{C,GA}$, (b) and (c) Variation of $I_{FSP,G}$ and $I_{BSP,G}$ respectively ($I_{FSP,G} = 0$ for $s = 6$ while $I_{BSP,G} = 0$ for $s = 4$ and 10), and (d) Variation of $I_{GA,G}$ ($I_{GA,G} = 0$ for $s = 4$ and 6).

By using the GA based optimization on the new objective function G for both the cantilever beam and the milling tower, it was seen that the method attains the global optimal solution for cases when number of sensors are not large, while both the FSP and BSP provided global optimal solution only in certain cases. Still the very low values of $I_{FSP,G}$ and $I_{BSP,G}$ indicate the closeness of the solutions from the sequential method to the global optimal values. Figure 12 compares the number of configurations evaluated for both the cantilever beam and the milling tower when using the different methods. As stated before, the optimization performed using an exhaustive search of all possible configurations become expensive as the number of sensors increases. The GA method is found to be computationally cheap for smaller number of sensors, while with an increase in sensors, it becomes expensive than the sequential methods. The BSP is found to be the most computationally efficient method while the FSP is better than GA only for larger number of sensors. The comparatively better estimation of G coupled with the low computational cost makes the BSP an efficient procedure for optimization in these particular case studies.

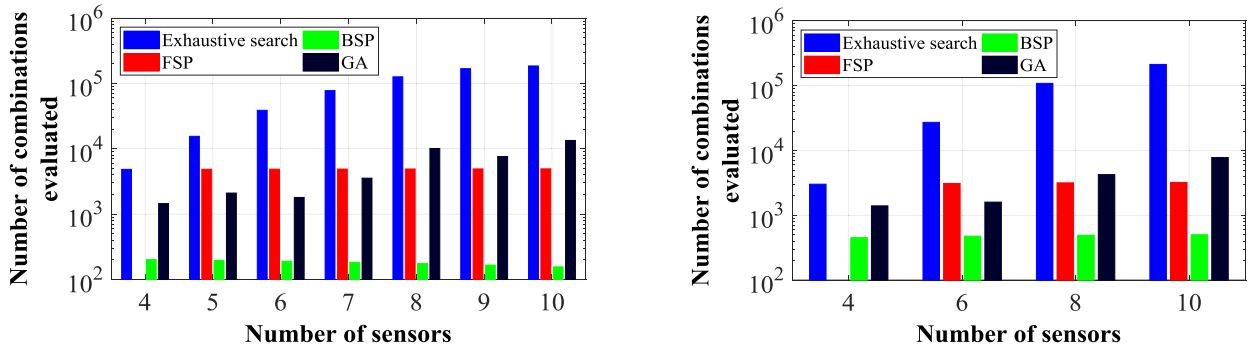

(a) (b)

Fig. 12. Comparison of number of sensor combinations evaluated for different optimization algorithms in case of; (a) The cantilever beam and (b) The milling tower

4. Conclusions

Expanding modal displacements obtained from a specific set of sensors to all the degrees of freedom can be essential in some specific structural health monitoring applications. Most of the commonly used conventional optimal sensor placement strategy aims at maximising the independence of the modal displacements at the sensor positions. However, this is not guaranteed to make the expanded mode shape close to the real mode shape under the presence of modelling error and measurement noise and to date, this specific problem has not been addressed. In this paper, the normal distance between the expanded and the real mode shape is proposed as a tool to measure their similarity. A new set of

optimal configurations were obtained by minimizing this normal distance. It was seen that the optimal normal distance increased significantly with an increase in measurement noise and modelling error. However, for a given modelling error and measurement noise, it was possible to improve the quality of modal expansion by increasing the number of sensors. It was found that the new optimal configuration when compared to the conventional optimal configuration based on linear independence of mode shapes was able to reduce the square of the normal distance by up to 24% and 40% respectively in case of the cantilever beam and the milling tower. Thus, the obtained sensor configuration ensures an expansion which is going to be as close as possible to the real mode shape. An example where this strategy might be particularly useful, is the design of an SHM system that is aiming at quantifying fatigue in structural members where strain gauges cannot be directly applied and thus modal expansion might be a possible way of indirectly obtaining stresses. However, the new optimal configuration may not be as effective as the conventional configuration for identification purposes. Also, it is to be understood that neither the new optimal configuration nor an increase in the number of sensors is able to balance the increase in the normal distance due to the increase in modelling error and measurement noise. At any rate, for a given measurement error, modelling noise and number of sensors, the new optimal solution will be the best available choice in cases where an expansion is required.

Acknowledgment

This study has received funding from the European Union's Horizon 2020 research and innovation programme under the Marie Skłodowska-Curie grant agreement No 721816. The authors would also like to thank Birla Carbon Italy SRL for all the help provided.

Appendix – A

A.1. Expected value of normal distance

Let λ represent an arbitrary scaling applied to $\boldsymbol{\Psi^l}$. As the Euclidian distance between two distinct vectors is a positive function, minimizing this function is equivalent to minimizing its square. For any sensor configuration **S**, square of the Euclidian distance f between vectors $\boldsymbol{\varphi^l}$ and $\lambda\boldsymbol{\Psi^l}$ is given by,

$$f\left(\boldsymbol{\varphi^l}, \lambda\boldsymbol{\Psi^l}\right)^2 = \left\|\boldsymbol{\varphi^l} - \lambda\boldsymbol{\Psi^l}\right\|^2$$

The expected value of square of the Euclidian distance is given as,

$$\begin{aligned} \mathrm{E}\left(f\left(\boldsymbol{\varphi^l}, \lambda\boldsymbol{\Psi^l}\right)^2\right) &= \mathrm{E}\left(\left\|\boldsymbol{\varphi^l} - \lambda\boldsymbol{\Psi^l}\right\|^2\right) \\ &= \mathrm{E}\left(\boldsymbol{\varphi^{l^T}}\boldsymbol{\varphi^l}\right) - 2\lambda\mathrm{E}\left(\boldsymbol{\varphi^{l^T}}\boldsymbol{\Psi^l}\right) + \lambda^2\mathrm{E}\left(\boldsymbol{\Psi^{l^T}}\boldsymbol{\Psi^l}\right) \end{aligned} \quad \text{(A.1.1)}$$

Differentiating Eq. (A1.1) with respect to λ (for a given $\boldsymbol{\varphi^l}$ and $\boldsymbol{\Psi^l}$) gives,

$$\frac{\mathrm{d}}{\mathrm{d}\lambda}\mathrm{E}\left(f\left(\boldsymbol{\varphi^l}, \lambda\boldsymbol{\Psi^l}\right)^2\right) = -2.\mathrm{E}\left(\boldsymbol{\varphi^{l^T}}\boldsymbol{\Psi^l}\right) + 2\lambda\mathrm{E}\left(\boldsymbol{\Psi^{l^T}}\boldsymbol{\Psi^l}\right)$$

$$\text{The stationary point of Eq. (A1.1), is } \lambda_c = \frac{\mathrm{E}\left(\boldsymbol{\varphi^{l^T}}\boldsymbol{\Psi^l}\right)}{\mathrm{E}\left(\boldsymbol{\Psi^{l^T}}\boldsymbol{\Psi^l}\right)}$$

Given the second derivative of Eq. (A1.1) with respect to λ,

$$\frac{\mathrm{d}^2}{\mathrm{d}\lambda^2}\mathrm{E}\left(f\left(\boldsymbol{\varphi^l}, \lambda\boldsymbol{\Psi^l}\right)^2\right) = 2\mathrm{E}\left(\boldsymbol{\Psi^{l^T}}\boldsymbol{\Psi^l}\right) > 0 \;\forall\; \boldsymbol{\Psi^l} \neq 0$$

The second derivative is always positive since the expanded mode shape $\boldsymbol{\Psi^l}$ can never be 0. Thus, $\lambda_c = \mathrm{E}\left(\boldsymbol{\varphi^{l^T}}\boldsymbol{\Psi^l}\right)/\mathrm{E}\left(\boldsymbol{\Psi^{l^T}}\boldsymbol{\Psi^l}\right)$ corresponds to the minimum value of the expected value of the Euclidean norm for mode shapes expanded using a particular sensor configuration **S**. This happens when the Euclidian norm becomes the normal distance between the two vectors. The square of the expected value of the normal distance G for a particular sensor configuration **S** and vectors $\boldsymbol{\varphi^l}$ and $\boldsymbol{\Psi^l}$ can thus be obtained by substituting λ_c in Eq. (A.1.1) as,

$$G = \mathrm{E}\left(f\left(\boldsymbol{\varphi^l}, \lambda_c\boldsymbol{\Psi^l}\right)^2\right) = \mathrm{E}\left(\boldsymbol{\varphi^{l^T}}\boldsymbol{\varphi^l}\right) - \frac{\left(\mathrm{E}\left(\boldsymbol{\varphi^{l^T}}\boldsymbol{\Psi^l}\right)\right)^2}{\mathrm{E}\left(\boldsymbol{\Psi^{l^T}}\boldsymbol{\Psi^l}\right)}$$

Appendix – B

B.1. Definition of $\mathrm{E}\left(\boldsymbol{\varphi}^{\boldsymbol{l}^{\mathrm{T}}}\boldsymbol{\varphi}^{\boldsymbol{l}}\right)$

From the relation between the real mode shape $\boldsymbol{\varphi}^{\boldsymbol{l}}$ and the numerical mode shape $\boldsymbol{\Phi}^{\boldsymbol{l}}$,

$$\begin{aligned}
\boldsymbol{\varphi}^{\boldsymbol{l}^{\mathrm{T}}}\boldsymbol{\varphi}^{\boldsymbol{l}} &= \left(\boldsymbol{\Phi}^{\boldsymbol{l}} - \boldsymbol{\varepsilon}^{\boldsymbol{l}}\right)^{\mathrm{T}}\left(\boldsymbol{\Phi}^{\boldsymbol{l}} - \boldsymbol{\varepsilon}^{\boldsymbol{l}}\right) \\
&= \boldsymbol{\Phi}^{\boldsymbol{l}^{\mathrm{T}}}\boldsymbol{\Phi}^{\boldsymbol{l}} - \boldsymbol{\Phi}^{\boldsymbol{l}^{\mathrm{T}}}\boldsymbol{\varepsilon}^{\boldsymbol{l}} - \boldsymbol{\varepsilon}^{\boldsymbol{l}^{\mathrm{T}}}\boldsymbol{\Phi}^{\boldsymbol{l}} + \boldsymbol{\varepsilon}^{\boldsymbol{l}^{\mathrm{T}}}\boldsymbol{\varepsilon}^{\boldsymbol{l}} \\
&= \boldsymbol{\Phi}^{\boldsymbol{l}^{\mathrm{T}}}\boldsymbol{\Phi}^{\boldsymbol{l}} - 2\boldsymbol{\Phi}^{\boldsymbol{l}^{\mathrm{T}}}\boldsymbol{\varepsilon}^{\boldsymbol{l}} + \boldsymbol{\varepsilon}^{\boldsymbol{l}^{\mathrm{T}}}\boldsymbol{\varepsilon}^{\boldsymbol{l}} \\
\mathrm{E}\left(\boldsymbol{\varphi}^{\boldsymbol{l}^{\mathrm{T}}}\boldsymbol{\varphi}^{\boldsymbol{l}}\right) &= \mathrm{E}\left(\boldsymbol{\Phi}^{\boldsymbol{l}^{\mathrm{T}}}\boldsymbol{\Phi}^{\boldsymbol{l}} - 2\boldsymbol{\Phi}^{\boldsymbol{l}^{\mathrm{T}}}\boldsymbol{\varepsilon}^{\boldsymbol{l}} + \boldsymbol{\varepsilon}^{\boldsymbol{l}^{\mathrm{T}}}\boldsymbol{\varepsilon}^{\boldsymbol{l}}\right) \\
&= \mathrm{E}\left(\boldsymbol{\Phi}^{\boldsymbol{l}^{\mathrm{T}}}\boldsymbol{\Phi}^{\boldsymbol{l}}\right) - 2\mathrm{E}\left(\boldsymbol{\Phi}^{\boldsymbol{l}^{\mathrm{T}}}\boldsymbol{\varepsilon}^{\boldsymbol{l}}\right) + \mathrm{E}\left(\boldsymbol{\varepsilon}^{\boldsymbol{l}^{\mathrm{T}}}\boldsymbol{\varepsilon}^{\boldsymbol{l}}\right) \\
&= \mathrm{E}\left(\left\|\boldsymbol{\Phi}^{\boldsymbol{l}}\right\|_2{}^2\right) - 2\boldsymbol{\Phi}^{\boldsymbol{l}^{\mathrm{T}}}\mathrm{E}\left(\boldsymbol{\varepsilon}^{\boldsymbol{l}}\right) + \mathrm{E}\left(\boldsymbol{\varepsilon}^{\boldsymbol{l}^{\mathrm{T}}}\boldsymbol{\varepsilon}^{\boldsymbol{l}}\right) \\
&= \mathrm{E}\left(\left\|\boldsymbol{\Phi}^{\boldsymbol{l}}\right\|_2{}^2\right) - 2\boldsymbol{\Phi}^{\boldsymbol{l}^{\mathrm{T}}}\mathrm{E}\left(\boldsymbol{\varepsilon}^{\boldsymbol{l}}\right) + \mathrm{E}\left({\varepsilon_1^l}^2 + {\varepsilon_2^l}^2 + \cdots + {\varepsilon_n^l}^2\right)
\end{aligned}$$

where, $\boldsymbol{\varepsilon}^{\boldsymbol{l}} = [\varepsilon_1^l \quad \varepsilon_2^l \quad \cdots \quad \varepsilon_n^l]^T$

$$\mathrm{E}\left(\boldsymbol{\varphi}^{\boldsymbol{l}^{\mathrm{T}}}\boldsymbol{\varphi}^{\boldsymbol{l}}\right) = \left\|\boldsymbol{\Phi}^{\boldsymbol{l}}\right\|_2{}^2 - 2\boldsymbol{\Phi}^{\boldsymbol{l}^{\mathrm{T}}}\mathrm{E}(\boldsymbol{\varepsilon}_{\mathbf{l}}) + \left({\sigma_{\varepsilon_1^l}}^2 + {\sigma_{\varepsilon_2^l}}^2 + \cdots + {\sigma_{\varepsilon_n^l}}^2\right) + \left({\mu_{\varepsilon_1^l}}^2 + {\mu_{\varepsilon_2^l}}^2 + \cdots + {\mu_{\varepsilon_n^l}}^2\right)$$

Since, the modelling error is 0 mean with the same standard deviation σ_ε at all the degrees of freedom,

$$\begin{aligned}
\mathrm{E}\left(\boldsymbol{\varphi}^{\boldsymbol{l}^{\mathrm{T}}}\boldsymbol{\varphi}^{\boldsymbol{l}}\right) &= \left\|\boldsymbol{\Phi}^{\boldsymbol{l}}\right\|_2{}^2 - 0 + n{\sigma_\varepsilon}^2 + 0 \\
&= n{\sigma_\varepsilon}^2 + \left\|\boldsymbol{\Phi}^{\boldsymbol{l}}\right\|_2{}^2
\end{aligned}$$

B.2. Definition of $\mathrm{E}\left(\boldsymbol{\Psi}^{\boldsymbol{l}^{\mathrm{T}}}\boldsymbol{\Psi}^{\boldsymbol{l}}\right)$

From the definition of experimental modal displacement, $\boldsymbol{\psi}^{\boldsymbol{l}} = \boldsymbol{\varphi}_{\boldsymbol{s}}^{\boldsymbol{l}} + \boldsymbol{\eta}^{\boldsymbol{l}} = \boldsymbol{\Phi}_{\boldsymbol{s}}^{\boldsymbol{l}} - \boldsymbol{\varepsilon}_{\boldsymbol{s}}^{\boldsymbol{l}} + \boldsymbol{\eta}^{\boldsymbol{l}} = \boldsymbol{\Phi}_{\boldsymbol{s}}^{\boldsymbol{l}} - \mathbf{N}^{\boldsymbol{l}}$

where, $\mathbf{N}^{\boldsymbol{l}} = \boldsymbol{\varepsilon}_{\boldsymbol{s}}^{\boldsymbol{l}} - \boldsymbol{\eta}^{\boldsymbol{l}}$ is the net difference of modelling error and measurement noise at the s sensor positions. Since both $\boldsymbol{\varepsilon}$ and $\boldsymbol{\eta}$ are assumed to be 0 mean Gaussian process with the same standard deviations σ_ε and σ_η at all the relevant degrees of freedom, $\mathbf{N}^{\boldsymbol{l}}$ will also be a 0 mean Gaussian process with variance matrix given as,

$$\boldsymbol{\Sigma}_{\mathbf{N}}{}^2 = {\sigma_{\mathrm{N}}}^2\mathbf{I}_{\mathbf{s}}$$

where, ${\sigma_{\mathrm{N}}}^2 = {\sigma_\varepsilon}^2 + {\sigma_\eta}^2$.

Now,

$$\begin{aligned}
\mathrm{E}\left(\boldsymbol{\psi}^{\boldsymbol{l}}\right) = \boldsymbol{\mu}_{\boldsymbol{\psi}^{\boldsymbol{l}}} &= \mathrm{E}\left(\boldsymbol{\Phi}_{\boldsymbol{s}}^{\boldsymbol{l}} - \mathbf{N}^{\boldsymbol{l}}\right) = \boldsymbol{\Phi}_{\boldsymbol{s}}^{\boldsymbol{l}} - \mathrm{E}\left(\mathbf{N}^{\boldsymbol{l}}\right) = \boldsymbol{\Phi}_{\boldsymbol{s}}^{\boldsymbol{l}} \\
\boldsymbol{\Psi}^{\boldsymbol{l}^{\mathrm{T}}}\boldsymbol{\Psi}^{\boldsymbol{l}} &= \boldsymbol{\psi}^{\boldsymbol{l}^{\mathrm{T}}}\mathbf{C}^{\mathrm{T}}\mathbf{C}\boldsymbol{\psi}^{\boldsymbol{l}} \qquad (\text{Since } \boldsymbol{\Psi}^{\boldsymbol{l}} = \mathbf{C}\boldsymbol{\psi}^{\boldsymbol{l}}) \\
\mathrm{E}\left(\Psi^{l^{\mathrm{T}}}\Psi^{l}\right) &= \mathrm{E}\left(\boldsymbol{\psi}^{\boldsymbol{l}^{\mathrm{T}}}\mathbf{C}^{\mathrm{T}}\mathbf{C}\boldsymbol{\psi}^{\boldsymbol{l}}\right) \\
&= \mathrm{E}\left(\left(\boldsymbol{\psi}^{\boldsymbol{l}} - \boldsymbol{\mu}_{\boldsymbol{\psi}^{\boldsymbol{l}}}\right)^{\mathrm{T}}\mathbf{C}^{\mathrm{T}}\mathbf{C}\left(\boldsymbol{\psi}^{\boldsymbol{l}} - \boldsymbol{\mu}_{\boldsymbol{\psi}^{\boldsymbol{l}}}\right)\right) + \boldsymbol{\mu}_{\boldsymbol{\psi}^{\boldsymbol{l}}}{}^{\mathrm{T}}\mathbf{C}^{\mathrm{T}}\mathbf{C}\boldsymbol{\mu}_{\boldsymbol{\psi}^{\boldsymbol{l}}} \qquad (\text{from Section B.2.1}) \\
&= \mathrm{E}\left(\mathrm{tr}\left(\mathbf{C}\left(\boldsymbol{\psi}^{\boldsymbol{l}} - \boldsymbol{\mu}_{\boldsymbol{\psi}^{\boldsymbol{l}}}\right)\left(\boldsymbol{\psi}^{\boldsymbol{l}} - \boldsymbol{\mu}_{\boldsymbol{\psi}^{\boldsymbol{l}}}\right)^{\mathrm{T}}\mathbf{C}^{\mathrm{T}}\right)\right) + \boldsymbol{\mu}_{\boldsymbol{\psi}^{\boldsymbol{l}}}{}^{\mathrm{T}}\mathbf{C}^{\mathrm{T}}\mathbf{C}\boldsymbol{\mu}_{\boldsymbol{\psi}^{\boldsymbol{l}}} \\
&= \mathrm{tr}\left(\mathbf{C}\mathrm{E}\left(\left(\boldsymbol{\psi}^{\boldsymbol{l}} - \boldsymbol{\mu}_{\boldsymbol{\psi}^{\boldsymbol{l}}}\right)\left(\boldsymbol{\psi}^{\boldsymbol{l}} - \boldsymbol{\mu}_{\boldsymbol{\psi}^{\boldsymbol{l}}}\right)^{\mathrm{T}}\right)\mathbf{C}^{\mathrm{T}}\right) + \boldsymbol{\mu}_{\boldsymbol{\psi}^{\boldsymbol{l}}}{}^{\mathrm{T}}\mathbf{C}^{\mathrm{T}}\mathbf{C}\boldsymbol{\mu}_{\boldsymbol{\psi}^{\boldsymbol{l}}} \\
&= \mathrm{tr}\left(\mathbf{C}\boldsymbol{\Sigma}_{\mathbf{N}}{}^{\mathbf{2}}\mathbf{C}^{\mathrm{T}}\right) + \boldsymbol{\mu}_{\boldsymbol{\psi}^{\boldsymbol{l}}}{}^{\mathrm{T}}\mathbf{C}^{\mathrm{T}}\mathbf{C}\boldsymbol{\mu}_{\boldsymbol{\psi}^{\boldsymbol{l}}} \text{ , where } \boldsymbol{\Sigma}_{\mathbf{N}}{}^{\mathbf{2}} \in \mathbb{R}^{s\,x\,s} \text{ is the covariance matrix of } \boldsymbol{\psi}^{\boldsymbol{l}}. \\
\mathrm{E}\left(\Psi^{l^{\mathrm{T}}}\Psi^{l}\right) &= \mathrm{tr}\left(\mathbf{C}\boldsymbol{\Sigma}_{\mathbf{N}}{}^{\mathbf{2}}\mathbf{C}^{\mathrm{T}}\right) + \boldsymbol{\Phi}_{\boldsymbol{s}}^{\boldsymbol{l}^{\mathrm{T}}}\mathbf{C}^{\mathrm{T}}\mathbf{C}\boldsymbol{\Phi}_{\boldsymbol{s}}^{\boldsymbol{l}}
\end{aligned}$$

B.2.1. Proof that $E\left(\left(\boldsymbol{\psi}^{\boldsymbol{l}}-\boldsymbol{\mu}_{\boldsymbol{\psi}^{\boldsymbol{l}}}\right)^{T}\boldsymbol{C}^{\boldsymbol{T}}\boldsymbol{C}\left(\boldsymbol{\psi}^{\boldsymbol{l}}-\boldsymbol{\mu}_{\boldsymbol{\psi}^{\boldsymbol{l}}}\right)\right)+\boldsymbol{\mu}_{\boldsymbol{\psi}^{\boldsymbol{l}}}{}^{T}\boldsymbol{C}^{\boldsymbol{T}}\boldsymbol{C}\boldsymbol{\mu}_{\boldsymbol{\psi}^{\boldsymbol{l}}}=E\left(\boldsymbol{\psi}^{\boldsymbol{l}^{T}}\boldsymbol{C}^{\boldsymbol{T}}\boldsymbol{C}\boldsymbol{\psi}^{\boldsymbol{l}}\right)$

$$
\begin{aligned}
&\mathrm{E}\left(\left(\boldsymbol{\psi}^{\boldsymbol{l}}-\boldsymbol{\mu}_{\boldsymbol{\psi}^{\boldsymbol{l}}}\right)^{T}\mathbf{C}^{T}\mathbf{C}\left(\boldsymbol{\psi}^{\boldsymbol{l}}-\boldsymbol{\mu}_{\boldsymbol{\psi}^{\boldsymbol{l}}}\right)\right)+\boldsymbol{\mu}_{\boldsymbol{\psi}^{\boldsymbol{l}}}{}^{\mathrm{T}}\mathbf{C}^{\mathrm{T}}\mathbf{C}\boldsymbol{\mu}_{\boldsymbol{\psi}^{\boldsymbol{l}}}\\
&=\mathrm{E}\left(\boldsymbol{\psi}^{\boldsymbol{l}^{\mathrm{T}}}\mathbf{C}^{\mathrm{T}}\mathbf{C}\boldsymbol{\psi}^{\boldsymbol{l}}-\boldsymbol{\psi}^{\boldsymbol{l}^{\mathrm{T}}}\mathbf{C}^{\mathrm{T}}\mathbf{C}\boldsymbol{\mu}_{\boldsymbol{\psi}^{\boldsymbol{l}}}-\boldsymbol{\mu}_{\boldsymbol{\psi}^{\boldsymbol{l}}}{}^{\mathrm{T}}\mathbf{C}^{\mathrm{T}}\mathbf{C}\boldsymbol{\psi}^{\boldsymbol{l}}+\boldsymbol{\mu}_{\boldsymbol{\psi}^{\boldsymbol{l}}}{}^{\mathrm{T}}\mathbf{C}^{\mathrm{T}}\mathbf{C}\boldsymbol{\mu}_{\boldsymbol{\psi}^{\boldsymbol{l}}}\right)+\boldsymbol{\mu}_{\boldsymbol{\psi}^{\boldsymbol{l}}}{}^{\mathrm{T}}\mathbf{C}^{\mathrm{T}}\mathbf{C}\boldsymbol{\mu}_{\boldsymbol{\psi}^{\boldsymbol{l}}}\\
&=\mathrm{E}\left(\boldsymbol{\psi}^{\boldsymbol{l}^{\mathrm{T}}}\mathbf{C}^{\mathrm{T}}\mathbf{C}\boldsymbol{\psi}^{\boldsymbol{l}}\right)-\mathrm{E}\left(\boldsymbol{\psi}^{\boldsymbol{l}^{\mathrm{T}}}\right)\mathbf{C}^{\mathrm{T}}\mathbf{C}\boldsymbol{\mu}_{\boldsymbol{\psi}^{\boldsymbol{l}}}-\boldsymbol{\mu}_{\boldsymbol{\psi}^{\boldsymbol{l}}}{}^{\mathrm{T}}\mathbf{C}^{\mathrm{T}}\mathbf{C}\mathrm{E}\left(\boldsymbol{\psi}^{\boldsymbol{l}}\right)+\boldsymbol{\mu}_{\boldsymbol{\psi}^{\boldsymbol{l}}}{}^{\mathrm{T}}\mathbf{C}^{\mathrm{T}}\mathbf{C}\boldsymbol{\mu}_{\boldsymbol{\psi}^{\boldsymbol{l}}}+\boldsymbol{\mu}_{\boldsymbol{\psi}^{\boldsymbol{l}}}{}^{\mathrm{T}}\mathbf{C}^{\mathrm{T}}\mathbf{C}\boldsymbol{\mu}_{\boldsymbol{\psi}^{\boldsymbol{l}}}\\
&=\mathrm{E}\left(\boldsymbol{\psi}^{\boldsymbol{l}^{\mathrm{T}}}\mathbf{C}^{\mathrm{T}}\mathbf{C}\boldsymbol{\psi}^{\boldsymbol{l}}\right)-\boldsymbol{\mu}_{\boldsymbol{\psi}^{\boldsymbol{l}}}{}^{\mathrm{T}}\mathbf{C}^{\mathrm{T}}\mathbf{C}\boldsymbol{\mu}_{\boldsymbol{\psi}^{\boldsymbol{l}}}-\boldsymbol{\mu}_{\boldsymbol{\psi}^{\boldsymbol{l}}}{}^{\mathrm{T}}\mathbf{C}^{\mathrm{T}}\mathbf{C}\boldsymbol{\mu}_{\boldsymbol{\psi}^{\boldsymbol{l}}}+\boldsymbol{\mu}_{\boldsymbol{\psi}^{\boldsymbol{l}}}{}^{\mathrm{T}}\mathbf{C}^{\mathrm{T}}\mathbf{C}\boldsymbol{\mu}_{\boldsymbol{\psi}^{\boldsymbol{l}}}+\boldsymbol{\mu}_{\boldsymbol{\psi}^{\boldsymbol{l}}}{}^{\mathrm{T}}\mathbf{C}^{\mathrm{T}}\mathbf{C}\boldsymbol{\mu}_{\boldsymbol{\psi}^{\boldsymbol{l}}}\\
&=\mathrm{E}\left(\boldsymbol{\psi}^{\boldsymbol{l}^{\mathrm{T}}}\mathbf{C}^{\mathrm{T}}\mathbf{C}\boldsymbol{\psi}^{\boldsymbol{l}}\right)
\end{aligned}
$$

B.3. Definition of $\mathrm{E}\left(\boldsymbol{\varphi}^{\boldsymbol{l}^{\mathrm{T}}}\boldsymbol{\Psi}^{\boldsymbol{l}}\right)$

$$\mathrm{E}\left(\boldsymbol{\varphi}^{\boldsymbol{l}^{\mathrm{T}}}\boldsymbol{\Psi}^{\boldsymbol{l}}\right)=\mathrm{E}\left(\boldsymbol{\varphi}^{\boldsymbol{l}^{\mathrm{T}}}\right)\mathrm{E}\left(\boldsymbol{\Psi}^{\boldsymbol{l}}\right)+\mathrm{tr}\left(\mathrm{cov}\left(\boldsymbol{\varphi}^{\boldsymbol{l}},\boldsymbol{\Psi}^{\boldsymbol{l}}\right)\right)$$

where $\mathrm{cov}\left(\varphi^{l},\Psi^{l}\right)$ is the covariance matrix between $\boldsymbol{\varphi}^{\boldsymbol{l}}$ and Ψ^{l}

$$
\begin{aligned}
\mathrm{E}\left(\boldsymbol{\varphi}^{\boldsymbol{l}^{\mathrm{T}}}\boldsymbol{\Psi}^{\boldsymbol{l}}\right)&=\mathrm{E}\left(\boldsymbol{\varphi}^{\boldsymbol{l}^{\mathrm{T}}}\right)\mathrm{E}\left(\mathbf{C}\boldsymbol{\psi}^{\boldsymbol{l}}\right)+\mathrm{tr}\left(\mathrm{cov}\left(\boldsymbol{\varphi}^{\boldsymbol{l}},\mathbf{C}\boldsymbol{\psi}^{\boldsymbol{l}}\right)\right)\\
&=\boldsymbol{\Phi}^{\boldsymbol{l}^{\mathrm{T}}}\mathbf{C}\boldsymbol{\Phi}_{\boldsymbol{s}}^{\boldsymbol{l}}+\mathrm{tr}\left(\mathrm{cov}\left(\boldsymbol{\varphi}^{\boldsymbol{l}},\mathbf{C}\boldsymbol{\psi}^{\boldsymbol{l}}\right)\right)\qquad\left(\text{Since }\mathrm{E}\left(\boldsymbol{\varphi}^{\boldsymbol{l}}\right)=\boldsymbol{\Phi}^{\boldsymbol{l}}\text{ and }\mathrm{E}\left(\boldsymbol{\psi}^{\boldsymbol{l}}\right)=\boldsymbol{\Phi}_{\boldsymbol{s}}^{\boldsymbol{l}}\right)\\
\mathrm{tr}\left(\mathrm{cov}\left(\boldsymbol{\varphi}^{\boldsymbol{l}},\mathbf{C}\boldsymbol{\psi}^{\boldsymbol{l}}\right)\right)&=\mathrm{tr}\left(\mathrm{E}\left(\left(\boldsymbol{\varphi}^{\boldsymbol{l}}-\boldsymbol{\mu}_{\varphi^{l}}\right)\left(\mathbf{C}\boldsymbol{\psi}^{\boldsymbol{l}}-\mathbf{C}\boldsymbol{\mu}_{\boldsymbol{\psi}^{\boldsymbol{l}}}\right)^{\mathrm{T}}\right)\right)\\
&=\mathrm{tr}\left(\mathrm{E}\left(\left(\boldsymbol{\Phi}^{\boldsymbol{l}}-\boldsymbol{\varepsilon}^{\boldsymbol{l}}-\boldsymbol{\Phi}^{\boldsymbol{l}}\right)\left(\boldsymbol{\Phi}_{\boldsymbol{s}}^{\boldsymbol{l}}-\boldsymbol{\varepsilon}_{\boldsymbol{s}}^{\boldsymbol{l}}+\boldsymbol{\eta}^{\boldsymbol{l}}-\boldsymbol{\Phi}_{\boldsymbol{s}}^{\boldsymbol{l}}\right)^{\mathrm{T}}\mathbf{C}^{\mathrm{T}}\right)\right)\\
&=\mathrm{tr}\left(\mathrm{E}\left(\left(-\boldsymbol{\varepsilon}^{\boldsymbol{l}}\right)\left(-\boldsymbol{\varepsilon}_{\boldsymbol{s}}^{\boldsymbol{l}}+\boldsymbol{\eta}^{\boldsymbol{l}}\right)^{\mathrm{T}}\mathbf{C}^{\mathrm{T}}\right)\right)\\
&=\mathrm{tr}\left(\mathrm{E}\left(\boldsymbol{\varepsilon}^{\boldsymbol{l}}\left(\boldsymbol{\varepsilon}_{\boldsymbol{s}}^{\boldsymbol{l}}-\boldsymbol{\eta}^{\boldsymbol{l}}\right)^{\mathrm{T}}\right)\mathbf{C}^{\mathrm{T}}\right)\\
&=\mathrm{tr}\left(\mathrm{E}\left(\boldsymbol{\varepsilon}^{\boldsymbol{l}}\boldsymbol{\varepsilon}_{\boldsymbol{s}}^{\boldsymbol{l}^{\mathrm{T}}}\right)\mathbf{C}^{\mathrm{T}}\right)\qquad\left(\text{Since }\mathrm{E}\left(\boldsymbol{\varepsilon}^{\boldsymbol{l}}\boldsymbol{\eta}^{\boldsymbol{l}^{\mathrm{T}}}\right)=0\text{, as they are uncorrelated}\right)\\
\mathrm{E}\left(\varphi^{l^{\mathrm{T}}}\Psi^{l}\right)&=\boldsymbol{\Phi}^{\boldsymbol{l}^{\mathrm{T}}}\mathbf{C}\boldsymbol{\Phi}_{\boldsymbol{s}}^{\boldsymbol{l}}+\mathrm{tr}\left(\mathrm{E}\left(\boldsymbol{\varepsilon}^{\boldsymbol{l}}\boldsymbol{\varepsilon}_{\boldsymbol{s}}^{\boldsymbol{l}^{\mathrm{T}}}\right)\mathbf{C}^{\mathrm{T}}\right)
\end{aligned}
$$

Appendix – C

C.1. G when using SEREP modal expansion

In case of SEREP expansion, $\mathbf{C}\boldsymbol{\Phi}_s^l = \boldsymbol{\Phi}^l$. Thus,

$$\boldsymbol{\Phi}^{l\mathrm{T}}\mathbf{C}\boldsymbol{\Phi}_s^l = \boldsymbol{\Phi}^{l\mathrm{T}}\boldsymbol{\Phi}^l = \left\|\boldsymbol{\Phi}^l\right\|_2^{\,2} \tag{C.1.1}$$

$$\boldsymbol{\Phi}_s^{l\mathrm{T}}\mathbf{C}^{\mathrm{T}}\mathbf{C}\boldsymbol{\Phi}_s^l = \left(\mathbf{C}\boldsymbol{\Phi}_s^l\right)^{\mathrm{T}}\mathbf{C}\boldsymbol{\Phi}_s^l = \boldsymbol{\Phi}^{l\mathrm{T}}\boldsymbol{\Phi}^l = \left\|\boldsymbol{\Phi}^l\right\|_2^{\,2} \tag{C.1.2}$$

The mode shape matrix $\boldsymbol{\Phi}^l$ can be partitioned based on the measured and unmeasured degrees of freedom as $\boldsymbol{\Phi}^l = \begin{bmatrix}\boldsymbol{\Phi}_s^{l\mathrm{T}} & \boldsymbol{\Phi}_d^{l\mathrm{T}}\end{bmatrix}$ where $\boldsymbol{\Phi}_d^l \in \mathbb{R}^{d\,x\,s}$ refers to the unmeasured degrees of freedom and $s + d = n$.

Now from Eq. (4),

$$\begin{aligned}\mathrm{tr}\left(\mathrm{E}\left(\boldsymbol{\varepsilon}^l\boldsymbol{\varepsilon}_s^{l\mathrm{T}}\right)\mathbf{C}^{\mathrm{T}}\right) &= \mathrm{tr}\left(\begin{bmatrix}\sigma_\varepsilon^{\,2}\mathbf{I_s}\\ \mathbf{O}\end{bmatrix}\mathbf{C}^{\mathrm{T}}\right) \text{ where } \mathbf{O} \in \mathbb{R}^{d\,x\,s} \text{ is a null matrix}\\ &= \mathrm{tr}\left(\begin{bmatrix}\sigma_\varepsilon^{\,2}\mathbf{I_s}\\ \mathbf{O}\end{bmatrix}\boldsymbol{\Phi_s}\left(\boldsymbol{\Phi_s}^{\mathrm{T}}\boldsymbol{\Phi_s}\right)^{-1}\begin{bmatrix}\boldsymbol{\Phi_s}^{\mathrm{T}} & \boldsymbol{\Phi_d}^{\mathrm{T}}\end{bmatrix}\right)\\ &= \sigma_\varepsilon^{\,2}\mathrm{tr}\left(\boldsymbol{\Phi_s}\left(\boldsymbol{\Phi_s}^{\mathrm{T}}\boldsymbol{\Phi_s}\right)^{-1}\boldsymbol{\Phi_s}^{\mathrm{T}}\right)\end{aligned}$$

Since $\mathrm{tr}\left(\boldsymbol{\Phi_s}\left(\boldsymbol{\Phi_s}^{\mathrm{T}}\boldsymbol{\Phi_s}\right)^{-1}\boldsymbol{\Phi_s}^{\mathrm{T}}\right) = m$,

$$\mathrm{tr}\left(\mathrm{E}\left(\boldsymbol{\varepsilon}^l\boldsymbol{\varepsilon}_s^{l\mathrm{T}}\right)\mathbf{C}^{\mathrm{T}}\right) = \sigma_\varepsilon^{\,2}m \tag{C.1.3}$$

If all the sensor noises are assumed to be identical,

$$\begin{aligned}\mathrm{tr}\left(\mathbf{C}\boldsymbol{\Sigma_N}^2\mathbf{C}^{\mathrm{T}}\right) &= \sigma_\mathrm{N}^{\,2}\mathrm{tr}\left(\mathbf{C}\mathbf{C}^{\mathrm{T}}\right)\\ &= \sigma_\mathrm{N}^{\,2}\mathrm{tr}\left(\boldsymbol{\Phi}\left(\boldsymbol{\Phi_s}^{\mathrm{T}}\boldsymbol{\Phi_s}\right)^{-1}\boldsymbol{\Phi_s}^{\mathrm{T}}.\boldsymbol{\Phi_s}\left(\boldsymbol{\Phi_s}^{\mathrm{T}}\boldsymbol{\Phi_s}\right)^{-1}\boldsymbol{\Phi}^{\mathrm{T}}\right)\\ &= \sigma_\mathrm{N}^{\,2}\mathrm{tr}\left(\begin{bmatrix}\boldsymbol{\Phi_s}\\ \boldsymbol{\Phi_d}\end{bmatrix}\left(\boldsymbol{\Phi_s}^{\mathrm{T}}\boldsymbol{\Phi_s}\right)^{-1}\begin{bmatrix}\boldsymbol{\Phi_s}^{\mathrm{T}} & \boldsymbol{\Phi_d}^{\mathrm{T}}\end{bmatrix}\right)\\ &= \sigma_\mathrm{N}^{\,2}\left(\mathrm{tr}\left(\boldsymbol{\Phi_s}\left(\boldsymbol{\Phi_s}^{\mathrm{T}}\boldsymbol{\Phi_s}\right)^{-1}\boldsymbol{\Phi_s}^{\mathrm{T}}\right) + \mathrm{tr}\left(\boldsymbol{\Phi_d}\left(\boldsymbol{\Phi_s}^{\mathrm{T}}\boldsymbol{\Phi_s}\right)^{-1}\boldsymbol{\Phi_d}^{\mathrm{T}}\right)\right)\\ &= \sigma_\mathrm{N}^{\,2}\left(m + \mathrm{tr}\left(\boldsymbol{\Phi_d}\left(\boldsymbol{\Phi_s}^{\mathrm{T}}\boldsymbol{\Phi_s}\right)^{-1}\boldsymbol{\Phi_d}^{\mathrm{T}}\right)\right)\end{aligned} \tag{C.1.4}$$

Substituting Eq. (C.1.1-C.1.4) in Eq. (3),

$$G = n\sigma_\varepsilon^{\,2} + \left\|\boldsymbol{\Phi}^l\right\|_2^{\,2} - \frac{\left(\left\|\boldsymbol{\Phi}^l\right\|_2^{\,2} + \sigma_\varepsilon^{\,2}m\right)^2}{\sigma_\mathrm{N}^{\,2}\left(m + \mathrm{tr}\left(\boldsymbol{\Phi_d}\left(\boldsymbol{\Phi_s}^{\mathrm{T}}\boldsymbol{\Phi_s}\right)^{-1}\boldsymbol{\Phi_d}^{\mathrm{T}}\right)\right) + \left\|\boldsymbol{\Phi}^l\right\|_2^{\,2}}$$

References

1. A.K. Pandey, M. Biswas, M.M. Samman, Damage detection from changes in curvature mode shapes, J. Sound Vib. 145 (1991) 321–332. doi:10.1016/0022-460X(91)90595-B.
2. Kondo, I., Hamamoto, T., 1996. Seismic Damage Detection of Multi-Story Buildings Using Vibration Monitoring, in: proc. of 11th World Conference on Earthquake Engineering, 988, Acapulco, Mexico.
3. F. Pelayo, A. Skafte, M.L. Aenlle, R. Brincker, Modal Analysis Based Stress Estimation for Structural Elements Subjected to Operational Dynamic Loadings, Exp. Mech. 55 (2015) 1791–1802. doi:10.1007/s11340-015-0073-6.
4. M. Tarpø, B. Nabuco, A. Skafte, J. Kristoffersen, J. Vestermark, S. Amador, R. Brincker, Operational modal analysis based prediction of actual stress in an offshore structural model, in: Procedia Eng., 2017: pp. 2262–2267. doi:10.1016/j.proeng.2017.09.234.
5. C. Papadimitriou, C.P. Fritzen, P. Kraemer, E. Ntotsios, Fatigue predictions in entire body of metallic structures from a limited number of vibration sensors using Kalman filtering, Struct. Control Heal. Monit. 18 (2011) 554–573. doi:10.1002/stc.395.
6. Dertimanis, V.K., Chatzi, E.N., Eftekhar Azam, S., Papadimitriou, C., 2016. Fatigue assessment in steel railway bridges using output only vibration measurements and partial structural information, in: proc. of Third International Conference on Railway Technology: Research, Development and Maintenance, 139, Sardinia, Italy. doi:10.4203/ccp.110.139.
7. P.C. Shah, F.E. Udwadia, A Methodology for optimal sensor locations for identification of dynamic, systems, J. Appl. Mech. 45 (1978) 188–196. doi:10.1115/1.3424225.
8. F.E. Udwadia, Methodology for Optimum Sensor Locations for Parameter Identification in Dynamic Systems, J. Eng. Mech. 120 (1994). doi:10.1061/(asce)0733-9399(1994)120:2(368).
9. D.C. Kammer, Sensor placement for on-orbit modal identification and correlation of large space structures, J. Guid. Control. Dyn. 14 (1991) 251–259. doi:10.2514/3.20635.
10. D.C. Kammer, Effects of noise on sensor placement for on-orbit modal identification of large space structures, J. Dyn. Syst. Meas. Control. 114 (1992) 436–443. doi:10.2514/6.1993-1704.
11. D.C. Kammer, Effect of model error on sensor placement for on-orbit modal identification of large space structures, J. Guid. Control. Dyn. 15 (1992) 334–341. doi:10.2514/3.20841.
12. M.I. Friswell, J.E. Mottershead, Finite element model updating in structural dynamics, Springer-Science and Business Media., 2013. doi:10.1007/978-94-015-8508-8.
13. C. Schedlinski, M. Link, An Approach to Optimal Pick-up and Exciter Placement, in: 14th Int. Modal Anal. Conf., 1996: pp. 376–382.
14. G. Heo, M.L. Wang, D. Satpathi, Optimal transducer placement for health monitoring of long span bridge, Soil Dyn. Earthq. Eng. 16 (1997) 495–502. doi:10.1016/S0267-7261(97)00010-9.
15. E.M. Hernandez, Efficient sensor placement for state estimation in structural dynamics, Mech. Syst. Signal Process. 85 (2017) 789–800. doi:10.1016/j.ymssp.2016.09.005.
16. S. Zhu, X.-H. Zhang, Y.-L. Xu, S. Zhan, Multi-Type Sensor Placement for Multi-Scale Response Reconstruction, Adv. Struct. Eng. 16 (2013). doi:10.1260/1369-4332.16.10.1779.
17. Y.L. Xu, X.H. Zhang, S. Zhu, S. Zhan, Multi-type sensor placement and response reconstruction for structural health monitoring of long-span suspension bridges, Sci. Bull. 61 (2016) 313–329. doi:10.1007/s11434-016-1000-7.

18. X.H. Zhang, S. Zhu, Y.L. Xu, X.J. Homg, Integrated optimal placement of displacement transducers and strain gauges for better estimation of structural response, Int. J. Struct. Stab. Dyn. 11 (2011) 581–602. doi:10.1142/s0219455411004221.
19. C. Papadimitriou, Y. Haralampidis, K. Sobczyk, Optimal experimental design in stochastic structural dynamics, Probabilistic Eng. Mech. 20 (2005) 67–78. doi:10.1016/j.probengmech.2004.06.002.
20. W. Ostachowicz, R. Soman, P. Malinowski, Optimization of sensor placement for structural health monitoring: a review, Struct. Heal. Monit. 18 (2019) 963–988. doi:10.1177/1475921719825601.
21. V. Mallardo, M.H. Aliabadi, Optimal sensor placement for structural, damage and impact identification: A review, SDHM Struct. Durab. Heal. Monit. 9 (2013) 287–323. doi:10.1007/s10336-016-1361-3.
22. Y. Ting-Hua, L. Hong-Nan, Methodology developments in sensor placement for health monitoring of civil infrastructures, Int. J. Distrib. Sens. Networks. 8 (2012). doi:10.1155/2012/612726.
23. L. Dongsheng, Sensor placement methods and evaluation criteria in structural health monitoring, Universität Siegen, 2012.
24. G.F. Gomes, S.S. da Cunha, P. da Silva Lopes Alexandrino, B. Silva de Sousa, A.C. Ancelotti, Sensor placement optimization applied to laminated composite plates under vibration, Struct. Multidiscip. Optim. 58 (2018) 2099–2118. doi:10.1007/s00158-018-2024-1.
25. T.G. Carne, C.R. Dohrmann, A modal test design strategy for model correlation, in: proc. of 13th International Modal Analysis Conference. (1995) 927–933, Tennessee, United States
26. R.J. Allemang, D.L. Brown, A correlation coefficient for modal vector analysis, in: proc. of First International Modal Analysis Conference. (1982) 110-116, Florida, United States.
27. Lenticchia, E., Ceravolo, R., Antonaci, P., 2018. Sensor Placement Strategies for the Seismic Monitoring of Complex Vaulted Structures of the Modern Architectural Heritage, Shock Vib., 3739690. doi:10.1155/2018/3739690.
28. T.H. Yi, H.N. Li, M. Gu, Optimal sensor placement for structural health monitoring based on multiple optimization strategies, Struct. Des. Tall Spec. Build. 20 (2011) 881–900. doi:10.1002/tal.712.
29. G.F. Gomes, F.A. de Almeida, P. da Silva Lopes Alexandrino, S.S. da Cunha, B.S. de Sousa, A.C. Ancelotti, A multiobjective sensor placement optimization for SHM systems considering Fisher information matrix and mode shape interpolation, Eng. Comput. (2018) 1–17. doi:10.1007/s00366-018-0613-7.
30. Murugan Jaya, M., Ceravolo, R., Matta, E., Zanotti Fragonara, L., 2018. Performance of Sensor Placement Strategies Used in System Identification Based on Modal Expansion, in: proc. of 9th European Workshop on Structural Health Monitoring, EWSHM-0080-2018, Manchester, United Kingdom.
31. E. Reynders, K. Maes, G. Lombaert, G. De Roeck, Uncertainty quantification in operational modal analysis with stochastic subspace identification: Validation and applications, Mech. Syst. Signal Process. 66–67 (2016) 13–30. doi:10.1016/j.ymssp.2015.04.018.
32. E. Reynders, R. Pintelon, G. De Roeck, Uncertainty bounds on modal parameters obtained from stochastic subspace identification, Mech. Syst. Signal Process. 22 (2008) 948–969. doi:10.1016/j.ymssp.2007.10.009.
33. M. Döhler, X.B. Lam, L. Mevel, Uncertainty quantification for modal parameters from stochastic subspace identification on multi-setup measurements, Mech. Syst. Signal Process. 36 (2013) 562–581. doi:10.1016/j.ymssp.2012.11.011.
34. M. Döhler, F. Hille, X.-B. Lam, L. Mevel, W. Rücker, Confidence Intervals of Modal Parameters during Progressive Damage Test, in: Linking Models and Experiments, Volume 2, 2011. doi:10.1007/978-1-4419-9305-2_17.

35. G. Tondreau, E. Reynders, A. Deraemaeker, Towards a more realistic modelling of the uncertainty on identified mode shapes due to measurement noise, J. P 305 (2011) 012002. doi:10.1088/1742-6596/305/1/012002
36. R.J. GUYAN, Reduction of stiffness and mass matrices, AIAA J. 3 (1965) 380–380. doi:10.2514/3.2874.
37. L.F.F. Miguel, R.C.R. de Menezes, L.F.F. Miguel, Mode Shape Expansion from Data-Based System Identification Procedures, Mecánica Comput. 25 (2006) 1593–1602.
38. K. Robert L, Reduction of structural frequency equations., AIAA J. 11 (1973) 892–892. doi:10.2514/3.6852.
39. J. O'Callahan, P. Avitabile, R. Riemer, System equivalent reduction expansion process (SEREP), in: proc. of 7th International Modal Analysis Conference. (1989) 29-37, Las Vegas, United States.
40. J. O'Callahan, L. Ping, A Non-Smoothing SEREP Process for Modal Expansion, in: proc. of 12th International Modal Analysis Conference. (1994) 232–238, Honolulu, Hawaii.
41. C. Papadimitriou, Pareto optimal sensor locations for structural identification, Comput. Methods Appl. Mech. Eng. 194 (2005) 1655–1673. doi:10.1016/j.cma.2004.06.043.
42. L. Yao, W.A. Sethares, D.C. Kammer, Sensor placement for on-orbit modal identification via a genetic algorithm, AIAA J. 31 (1993). doi:10.2514/3.11868.
43. K. Deep, K.P. Singh, M.L. Kansal, C. Mohan, A real coded genetic algorithm for solving integer and mixed integer optimization problems, Appl. Math. Comput. 212 (2009) 505–518. doi:10.1016/j.amc.2009.02.044.
44. H. Randy L, H. Sue Ellen, Practical genetic algorithms, 2nd ed., John Wiley & Sons, Inc., Hoboken, New Jersey, 1998.
45. Global Optimization Toolbox User's Guide R2018b, The MathWorks, Inc. 3 Apple Hill Drive Natick, MA 01760-2098, 2018. https://www.mathworks.com/help/pdf_doc/optim/optim_tb.pdf.
46. D. E Goldberg, Genetic Algorithms in Search, Optimization and Machine Learning, 1st ed., Addison-Wesley Publishing Company, 1989.
47. R. Brincker, C.E. Ventura, Introduction to Operational Modal Analysis, 1st ed., John Wiley & Sons Ltd, West Sussex, United Kingdom, 2015. doi:10.1002/9781118535141.